Materials Advances

ROYAL SOCIETY OF CHEMISTRY

REVIEW

View Article Online
View Journal | View Issue

Cite this: *Mater. Adv.*, 2022, 3, 810

Insights into the diverse precursor-based micro-spherical hard carbons as anode materials for sodium–ion and potassium–ion batteries

Nagmani, Ashwani Tyagi and Sreeraj Puravankara *

In the past decade, the growth of the renewable energy sector worldwide and the depleting resources for Li-ion battery (LIB) technology have pushed the case for complementary storage technologies, especially for stationary energy storage. Sodium-ion batteries (SIB) are on the verge of large-scale commercialization, and potassium-ion battery (PIB) technology is a relative newcomer in the field of future storage technologies. Suitable, low-cost, and environmentally benign commercial electrode materials are the most researched battery systems in this context. Like LIBs, carbonaceous materials can potentially be the first commercial anode material for sodium-ion and potassium-ion batteries. Micro-spherical hard carbons (MSHCs) have the added advantage of higher packing density and low surface area to volume ratio with good structural stability. The metal-ion storage capacity is critically dependent on the morphology, surface area, surface defects, degree of graphitization, and porosity. The review addresses the influence of diverse precursors and synthesis conditions on the electrochemical storage of micro-spherical hard carbons, focusing on the storage-capacity and storage-mechanism correlation and the precursors' structural influence in designing anodes for sustainable, green, and safe SIBs and PIBs.

Received 16th August 2021,
Accepted 30th November 2021

DOI: 10.1039/d1ma00731a

rsc.li/materials-advances

Introduction

Sodium-ion batteries (SIBs) and potassium ion batteries (PIBs) are now universally viewed as the most encouraging and efficient complementary energy storage devices after the development of high energy and power density lithium-ion batteries (LIBs).[1,2] Portable electronic devices (PEDs), electric vehicles (EVs), and renewable energy storage sectors have already successfully implemented LIB technology.[3–6] The limited natural abundance of lithium compared to sodium and potassium will challenge LIB technology to meet future energy storage demands. The world has already geared up for e-mobility for transportation and renewable energy sources for

School of Energy Science & Engineering, Indian Institute of Technology Kharagpur, Kharagpur-721302, West Bengal, India. E-mail: sreeraj@iitkgp.ac.in; Tel: +91-3222 260801

Nagmani

Nagmani is a doctoral fellow at the School of Energy Science and Engineering, Indian Institute of Technology Kharagpur. He received his MTech and BTech in Energy Engineering from Central University of Jharkhand Ranchi, India, in 2016. His current research is focused on high-capacity carbonaceous anodes for alkali-ion batteries and the fabrication of high-energy-density sodium-ion batteries.

Ashwani Tyagi

Ashwani Tyagi is a doctoral fellow at the School of Energy Science and Engineering, Indian Institute of Technology Kharagpur. In 2017, he received his MTech and BTech in Nanotechnology from Central University of Jharkhand, Ranchi, India. His doctoral research is on cathode materials for alkali-ion batteries.

power production, where large-scale stationary storage devices have become irrelevant.[1,7,8] The complementary storage technologies of SIBs,[2,9,10] and PIBs[11,12] have attracted the interest of researchers due to their low cost, better raw material distribution, and most importantly, a similar cell fabrication process to the well-developed LIB technology. In recent years, many functionalized materials have been reported as anodes,[10,13–15] cathodes,[16–19] and electrolytes[20–24] for SIBs and PIBs. Carbon-based anode materials have always played a significant role in alkali–ion batteries due to low-cost fabrication, abundance, and exclusively tunable electronic and structural properties. LIBs mainly use graphite as anode materials and are technically challenging for SIB/PIB anode applications. Sodium-rich graphite insertion compounds (GICs) such as NaC_6, and NaC_8[25–28] do not exist due to the higher ionic radius of Na^+ (227 pm) *versus* Li^+ (182 pm) and positive adsorption energy during the intercalation process.[28]

In fully lithiated graphite, LiC_6 shows a theoretical capacity of 372 mA h g^{-1}, and various studies have indicated sodium intercalation compounds such as NaC_{70}, NaC_{64}, NaC_{60}, and NaC_{15} showing low sodium insertion capacities of 31, 35, 70, and 130 mA h g^{-1}, respectively.[29–31] Incidentally, PIBs utilize graphite as an anode material and deliver a capacity close to the theoretical capacity of 279 mA h g^{-1} by forming an insertion compound, KC_8.[32,33] Hard carbons from various diverse precursors have emerged as an alternative to graphite in SIBs and PIBs. Hard carbons (HCs) as anode materials deliver a relatively higher reversible capacity and cycling stability than graphite due to (i) the wider interlayer distance in the range of 3.7–4.2 nm[34,35] for accessible accommodation of Na^+/K^+ ions between the layers of graphitic domains, and (ii) the diverse storage mechanisms for Na^+/K^+ ions including adsorption, insertion, and pore filling. In this regard, non-graphitizable hard carbons (HCs) have been studied extensively for SIBs and PIBs.[29,30,36,37] The approach involves tailoring the morphology of HC's to provide unique physical and chemical properties, high ionic conductivity, thermal conductivity, and mechanical properties. Their unique structure provides high packing density and low surface area-to-volume ratio with good structural stability.[38,39] A few diverse synthetic techniques such as the microwave-assisted method,[38,40,41] hydrothermal,[36,42–45] solvothermal,[46,47] and other new routes[48–51] were employed for HC synthesis. Their electrochemical performance improved by tweaking the porosity, degree of graphitization, and the materials' microstructure. The HCs reported to date for Na/K storage have shown low initial coulombic efficiency (ICE). The majority of the capacities are at low potentials near the alkali metal plating potential, leading to inherent safety issues. Micro-spherical hard carbons (MSHCs) provide an alternative, as the morphology can provide optimum surface-controlled phenomena, improve mobile ion kinetics, and enhance electronic conductivity. Micro-spherical hard carbons synthesized using sugar-based carbohydrates,[36,38,52,53] renewable bio-sources,[49,50,54,55] and plastic wastes[56–58] were reported to reveal significant scalability benefits, cost-effectiveness, and environmental sustainability. This review focuses on how synthetic techniques and diverse carbon precursors influence the morphology, porosity, and electrochemical performance of micro-spherical hard carbons as anode materials for SIBs and PIBs. Efforts to correlate the precursor choice, the material structure analysis to the storage mechanism, and the electrochemical performance in the sodium/potassium batteries were made to provide insights into how micro-spherical hard carbons can play a significant role in engineering an efficient anode material for Na^+/K^+ storage.

Sreeraj Puravankara

Sreeraj Puravankara completed his PhD from NRW Graduate School of Chemistry, University of Muenster, Germany, in 2005. He did his postdoctoral work at the University of Muenster, Max Planck Institute for Solid-State Research, Stuttgart, and the Technical University of Munich before joining the School of Energy Science and Engineering as an Assistant Professor at the Indian Institute of Technology Kharagpur, India. His research focuses on experimental and theoretical studies of functional materials for electrochemical energy storage.

Material characterization of MSHCs

Hard carbons are disordered carbonaceous materials where long-range graphitic-type layer ordering is missing even at temperatures above 2000 °C. Short-range nano-micro graphitic domains may exist depending on the precursor used and the final carbonization temperature. The carbonization of precursors with strongly cross-linked structures results in locally stacked, highly turbostratic layered hard carbons.[59]

Several characterization tools are used for the morphological and structural analysis of hard carbon. The characteristic PXRD pattern of a disordered hard carbon shows two broad peaks at around 2θ–23°, and 43° (shifted to a lower 2θ as compared to graphite) indexed to the crystallographic planes (002) and (100). The broadening of the (002) peak at lower carbonization temperature indicates a larger interlayer spacing (Fig. 1a) due to increasing structure disorder. The *in situ* PXRD studies have revealed the sodium–ion storage mechanism in disordered hard carbons.[60,61] The degree of disordering of the hard carbon can be well understood by Raman spectroscopy.[62,63] The "D" bands that appear in the range of 1340–1360 cm^{-1} suggest defects in the structure, whereas the "G" bands at around 1580–1600 cm^{-1} are typical of graphitic layers. The D and G bands' intensity/relative area ratio (I_D/I_G) is directly proportional to the carbon structure disorder and inversely proportional to the graphitic domain size. Jin *et al.*[64] reported that the decrease in the I_D/I_G ratio is a direct indicator of an increase in

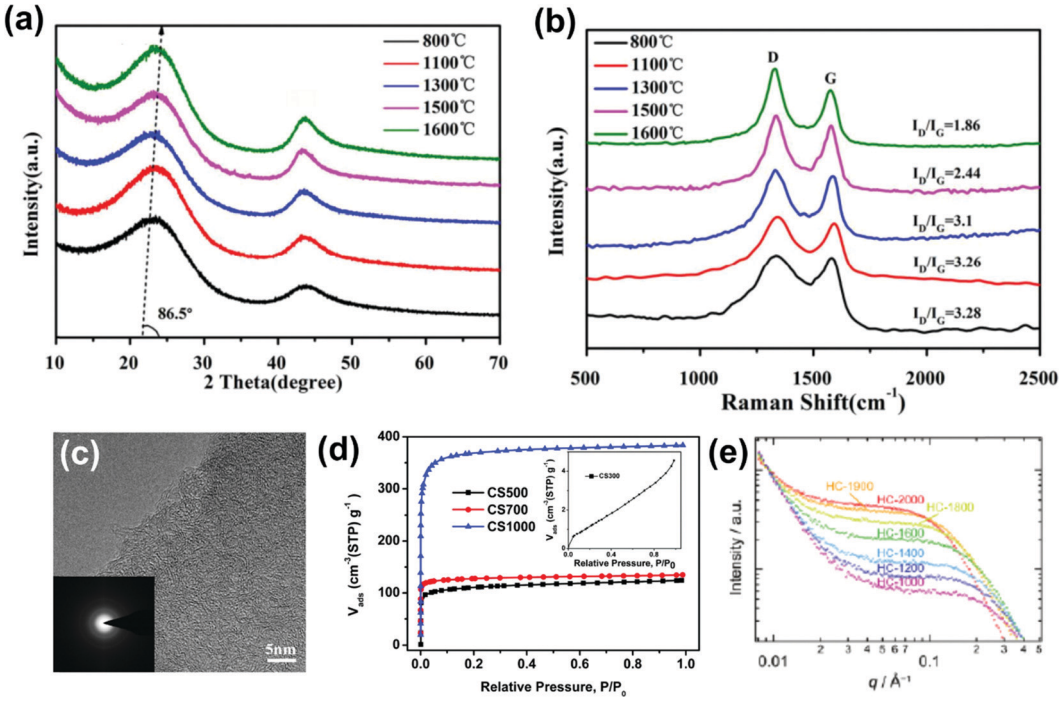

Fig. 1 Structural analysis of hard carbon: (a) XRD patterns, (b) Raman spectra at carbonization temperatures from 800 to 1600 °C, (c) HR-TEM image of HC at 1300 °C. Reprinted (adapted) with permission.[64] Copyright 2018, American Chemical Society. (d) Nitrogen adsorption isotherm of HC (the inset shows the isotherm of HC at 300 °C). Reproduced with permission.[38] Copyright 2014, Royal Society of Chemistry. (e) SAXS profile of HC *vs.* different carbonization temperatures. Reproduced with permission.[47] Copyright 2019, Wiley.

the short-range ordering in the structure with the rise in carbonization temperature, as shown in Fig. 1b.

High-Resolution Transmission Electron Microscopy (HR-TEM) can reveal the microstructure evolution of hard carbons at the nanoscale. The HR-TEM image shows the curved, randomly oriented,[65] and stacked graphene layer from which the curvature and the interlayer spacing of the graphene layers can be qualitatively obtained.[66] Fig. 1c displays an HR-TEM image of hard carbon synthesized from resorcinol formaldehyde *via* the hydrothermal method at 1300 °C showing curved short-range ordered graphitic domains. The diffuse ring observed in the selected area electron diffraction (SAED) image confirms carbon's amorphous phase.[64]

The most significant properties of hard carbon, such as porosity and surface area, play a vital role in the sodium insertion mechanism into the pores and initial irreversible losses due to the formation of the solid electrolyte interface (SEI) layer. The gas adsorption and desorption isotherm using N_2, CO_2, and Ar molecules on the carbonaceous surface can provide valuable insight into the sample's porosity. The Brunauer–Emmett–Teller (BET) technique is a well-known technique for measuring the surface area of carbonaceous materials with micropores.[67] Chen *et al.*[38] fabricated micro-spherical hard carbons with type I isotherms that indicate the microporosity of the material (Fig. 1d).

Small-angle X-ray scattering (SAXS) can complement the analysis of the hard carbon microstructure. The low angle scattering for hard carbon can provide information about the surface porosity of open and closed pores. Morikawa *et al.*[47] performed SAXS of hard carbon synthesized at different carbonization temperatures. The scattering shift to the lower scattering vector (q) region with the rise in carbonization temperature corresponds to the nanostructure and nanopores in the hard carbon structure (Fig. 1e). Besides, *in situ* SAXS uses the transmission mode to understand the sodium insertion mechanism into the micropores at the low voltage plateau region in SIBs.[68,69]

Electrochemical storage mechanism models

Understanding the ion storage mechanisms in the host's hard carbon structure is critical to its fundamental design and performance as an anode material. Fig. 2 depicts the schematic of the storage electrochemistry of SIBs/PIBs and the plausible storage mechanisms. During the charging process, the positive electrode releases Na^+/K^+ ions that move to the negative electrode through the electrolyte and are adsorbed/intercalated into the negative electrode; the Na^+/K^+ ions return to the positive electrode during discharge through desodiation/depotassiation. The freed-up electrons from the redox reaction at the electrode power the external load in SIBs and PIBs.

Na–ion storage mechanism

Several contradicting Na–ion storage mechanism models have been proposed in the last two decades in attempts to understand the electrochemical behavior of HCs for SIBs.[21,31,34,47]

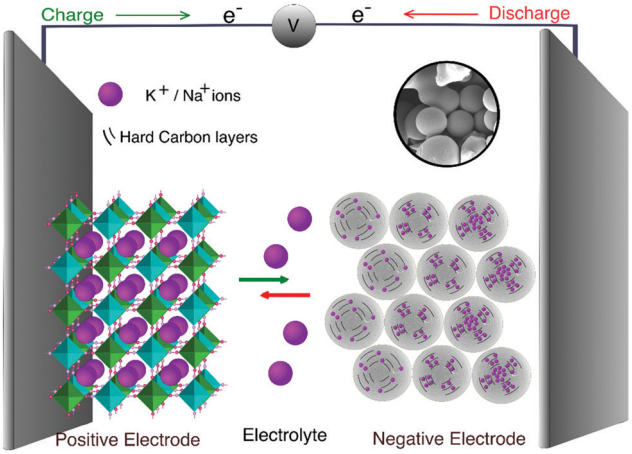

Fig. 2 Schematic showing the ion chemistry and the plausible storage mechanisms during the charge/discharge of MSHC as anode materials for SIBs and PIBs.

Many researchers have adopted the proposed "house of cards model" by Stevens and Dahn as the model structure to investigate the Na–ion storage mechanism using different characterization tools.[70,71] This model suggests an "intercalation–adsorption" mechanism as the defect-assisted interaction of ions in the pseudo-graphitic region at a higher voltage ($> \sim 0.1$ V), corresponding to the slope related capacity (SRC), whereas ion insertion into micropores occurs at a lower voltage ($< \sim 0.1$ V), resulting in a plateau-related capacity (PRC). Subsequently, Xiao *et al.*[72] proposed an "adsorption–intercalation" mechanism and suggested that the SRC was due to the Na ion's adsorption on the defect surface. In contrast, PRC was related to Na–ion insertion into graphite-like microcrystallites. The schematic mechanism of adsorption-intercalation and intercalation–adsorption are shown in Fig. 3a and b. Komaba *et al.*[21] applied *ex situ* XRD in the voltage range of 0.1 to 2 V and showed that the (002) peak shifted to a lower 2θ angle during discharge and regained its original position on reversible Na–ion removal during the charging process. Ji *et al.*[73–75] assumed that the PRC at a low potential is related to Na–ion insertion between the graphene sheets followed by Na–ions filling the pores of the carbon structure ("intercalation–filling" mechanism). The SRC is from the Na–ion storage at defect surfaces and edges.

The sodium plating during discharge in the plateau region is a significant concern investigated at various stages between 2 V and 0 V (Fig. 3c) by Qiu *et al.*[54] The solid-state nuclear magnetic resonance (SSNMR) studies during the discharge process revealed metallic/pseudo-metallic sodium during the Na-ion pore filling process. Fig. 3d shows the NMR spectra of hard carbon at various stages (II, III, and IV) of discharge. During discharge till 0 V, from II to III stage, no evidence of metal Na was observed but a sharp peak near −10 ppm is related to the sodium present on the surface of the electrode from the electrolyte salt. Electron paramagnetic/spin resonance (EPR/ESR) is a valuable tool for detecting sodium metal clusters during the discharge process. As the discharge proceeds from stage II to IV, the delocalized electron distribution at the Fermi level increases, resulting in the EPR signal's appearance, which gradually becomes intense. After the over-discharge of hard carbon below 0 V, the EPR signal gets divided into Lolunsi (broad peak) and Dysonian (sharp shoulder peak) line shapes. The sharp Dysonian line shape, which corresponds to metallic sodium deposition, only appears for the over-discharged electrode (Fig. 3e).

The sodium–ion storage mechanism in HCs involves two distinct voltage regions, SRC above 0.1 V and PRC below 0.1 V. Jin *et al.*[64] presented a new "three-phase" structure model for MSHC as illustrated in Fig. 3f and g. SRC corresponds to the adsorption capacity (AC) of Na–ions at the defect surface, and PRC has two parts based on the Na–ion diffusion coefficient, assigned to the intercalation capacity (IC) and pore-filling capacity (PFC). During insertion, the storage mechanism and the SRC and PRC contributions will depend upon the carbonization temperatures, surface defects/atoms, and types of pores in the hard carbon.[21] Komaba *et al.*[76] reported the new mechanism for sucrose-based hard carbon and suggested that the SRC is related to the defect-assisted adsorption at the edge of the graphitic planes and defect-assisted insertion into graphitic layers. In contrast, the PRC is due to the insertion followed by micropore filling, leading to pseudo-metallic clusters. A similar mechanism is supported by MSHC prepared from sucrose *via* the microwave-assisted solvothermal method.[77] In 2020, Komaba's group[78] reported that the capacity in the voltage range of 0.25 to 2 V was due to insertion into the large interlayer space close to the defects in the sp^2 carbon layer, whereas the lower voltage (0.25 to 0.002 V)-based capacity corresponds to the pseudometallic clustering of Na metal in micropores. Recently, S. Huang *et al.*[79] reported the four-stage mechanism model for 3-D hierarchical porous hard carbon for SIBs. The combined quasi-in-situ synchrotron XRD and *in situ* Raman investigation revealed the coexistence of different storage sites and processes within specific potential ranges. They attributed adsorption (stage-I, 2.5–1.0 V), defect adsorption and the beginning of intercalation (stage-II, 1.0–0.128 V), intercalation and nano-pore filling (stage-III, 0.128∼ (−0.0375) V), and surface overpotential deposition (stage-IV, −0.0329 V) as storage mechanisms. The storage mechanism models are still under scrutiny and more work in these directions are required to get a more refined storage-mechanism model.

K-ion storage mechanism

Earlier studies suggest various storage mechanisms of Li/Na ion in addition to intercalation, such as chemisorption on surface heteroatoms, metal nanopore filling, intercalation between graphene layers.[80–82] Potassium ion storage mechanisms in carbon-based materials mainly follow a "mixed potassium storage mechanism," which involves adsorption, pore filling, and intercalation.[83–92] To investigate the K-ion storage mechanism in partially graphitized hard carbon (NGHC), J. Hu *et al.*[84] carried out the cyclic voltammetry (CV) measurement in the scan rate range of 0.1 to 10 mV s^{-1}. The relationship between peak current density and scan rate revealed that

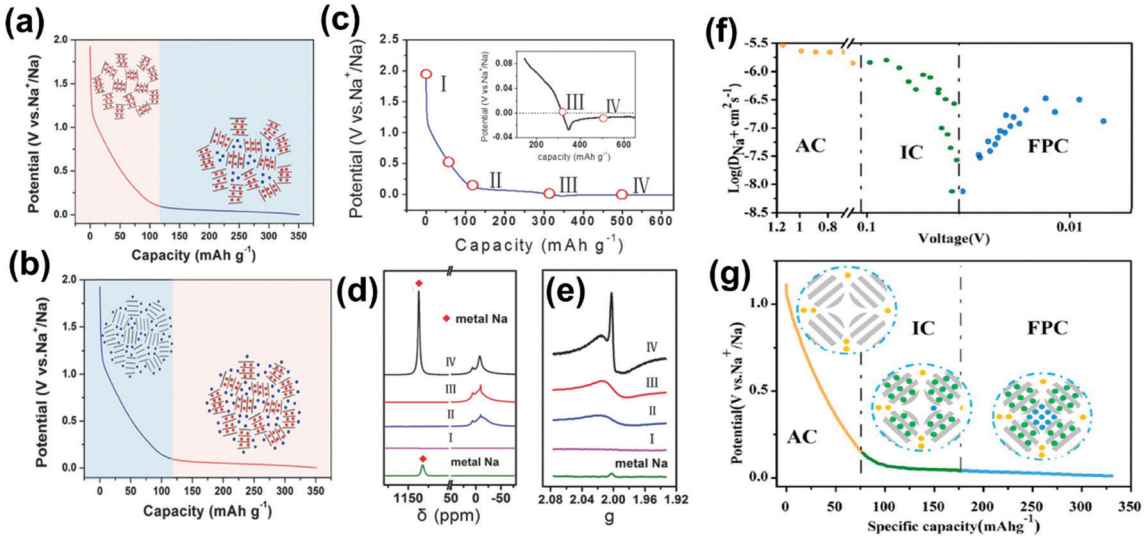

Fig. 3 (a) Mechanisms for Na–ion storage in hard carbon: (a) ''intercalation–adsorption'' mechanism, (b) ''adsorption–intercalation'' mechanism. (c) The discharge–charge curve for the HC-1300 electrode showing various stages of sodiation. (d) Na MAS NMR of HC-1300. (e) The EPR spectra of the HC-1300 electrode at different discharge states between −0.03 and 2.0 V. Reproduced with permission.[54] Copyright 2019, Wiley. (f) Na–ion diffusion coefficients calculated from the galvanostatic intermittent titration (GITT) technique curve of the HC electrode. (g) Schematic illustration of the mechanisms for Na–ion storage in hard carbon. Reprinted (adapted) with permission.[64] Copyright 2018, American Chemical Society.

potassium storage in NGHC is dominated by diffusion-controlled processes and shows defect adsorption in the sloping high-potential region. The *ex situ* Raman spectra were obtained to verify the mixed K-ion storage mechanism, as shown in Fig. 4a. The charge–discharge curve of the first cycle is illustrated in Fig. 4c, showing different storage possibilities in the voltage range from 0 V to 3 V, and the corresponding I_D/I_G ratios are shown in Fig. 4b. A gradual increase in the slope of I_D/I_G was observed at the high-potential region. A sharp change was observed in the low-potential region, which indicated adsorption in the high-potential region in disordered carbon and the intercalation of K ions in the graphitic domain in the low potential region of NGHC. Li Tao *et al.*[93] correlated the storage mechanism of K ions in soybeans-derived hard carbon with different morphologies. Fig. 4e–g shows that higher KOH activation temperatures can decrease the inter-carbon layer distance, resulting in other K-ion storage mechanisms. Fig. 4e indicates that adsorption dominated K-storage, whereas Fig. 4f and g shows the mixed intercalation and adsorption mechanism. The K^+ storage mechanism for soybean-derived hard

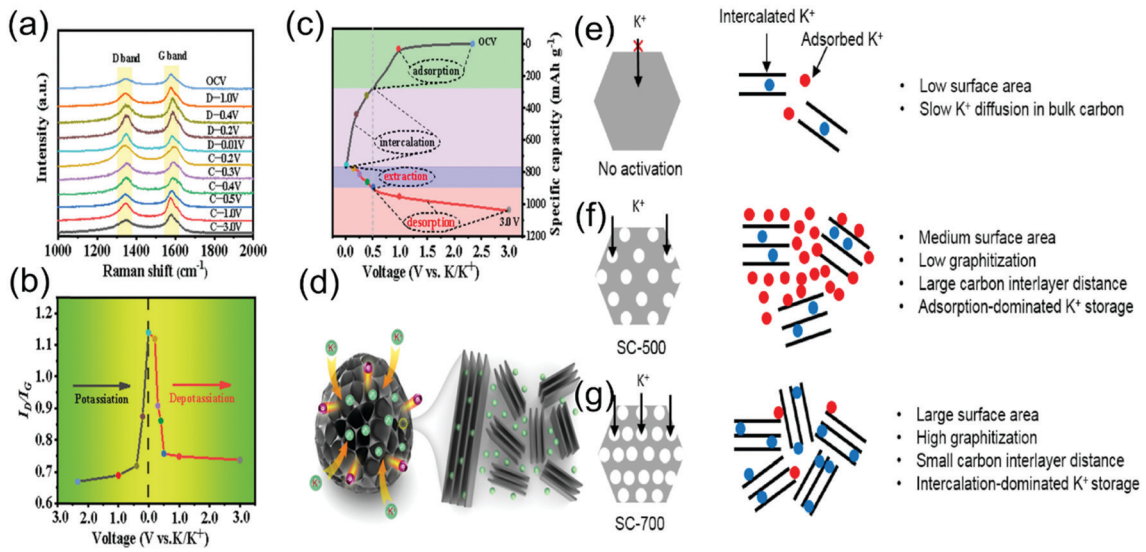

Fig. 4 (a) *Ex situ* Raman spectra (depotassiation), (b) the corresponding relative I_D/I_G changes at the first cycle of hard carbon, (c) charge–discharge curve, (d) schematic illustration of potassium ion storage in hard carbon. Reproduced with permission.[84] Copyright 2020, Elsevier. (e)–(g) Schematics for the K-ion storage mechanism in soybeans-derived hard carbon at low, medium, and high temperatures with increasing graphitization levels, respectively. Reproduced with permission.[93] Copyright 2020, Elsevier.

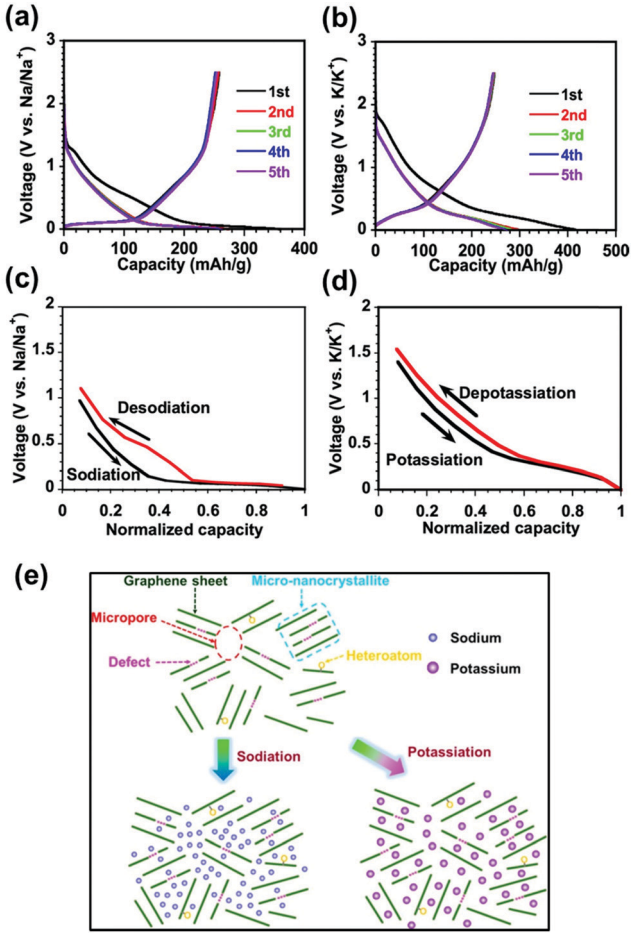

Fig. 5 The charge–discharge profile of sugar-based hard carbon in the (a) Na and (b) K metal–ion batteries. A comparison of the insertion/extraction behaviors in (c) SIB and (d) KIB showing the sloping and plateau regions. (e) Storage sites for sodiation, and potassiation in hard carbon. Reprinted (adapted) with permission.[94] Copyright 2021, American Chemical Society.

carbon investigated by Li Tao *et al.*[93] was similar to the report by J. Hu *et al.*[84] and truly justified the mixed intercalation and adsorption mechanism. Further, *ex situ* synchrotron radiation XRD confirmed the existence of K-metal at 0 V and implied the nanopore filling process at this stage. Therefore, the suggested model for K-ion storage indicated "adsorption, adsorption/intercalation, intercalation/pore-filling, and overpotential deposition. When discharged to 0 V, metal deposition due to the surface overpotential can lead to dendrite formation. The hierarchical porosity structure of NHPC could further inhibit the formation of dendrites, improving the safety of the cell.

Komaba *et al.*[76] reported that the discharge curve in the K cell consists of two sloping regions and no plateau region. The K-ions were inserted into the interlayer space at higher potential and internal pores at lower potential regions. Later, the same group[78] proposed a charge–discharge profile mechanism with three sloping voltage ranges (0.002–0.2 V), (0.2–0.7 V) (0.7–2 V) *vs.* K/K^+. At lower carbonization temperatures (700–900 °C), K-ion insertion into the larger intralayer space and at higher carbonization temperatures (1100–2000 °C), K-ion intercalation into the narrow interlayer graphitic planes dominate with negligible capacity contribution from pseudometallic clustering of potassium. S. Huang *et al.*[79] performed *in situ* Raman spectroscopy to determine the stages of the potassium insertion process. At OCV, the typical characterization peaks of N-doped hard porous carbon (NHPC) were D band (1350 cm^{-1}) and G band (1589 cm^{-1}), and during the first discharge from OCV to 1.2 V, the intensity and position of D and G peaks did not change significantly to indicate any insertion of K-ion into the interlayer space of NHPC, but a small amount of K-ions was adsorbed at the surface sites. At 0.25 V, D and G peaks shifted to the left, suggesting the K-ion insertion into the interlayer space (intercalation), and further, the disappearance of the D peak indicated the K-ion adsorbed at defect sites.

A unified storage mechanism model is challenging and is a work in progress while correlating the structural properties of HC with the electrochemical performance in SIBs and PIBs. Recently, Yong Huang and co-worker[94] reported a better understanding of alkali metal ion storage in the hard carbon. In SIBs (from the 2nd cycle), a slope above 0.1 V and a plateau near 0 V (Fig. 5a) indicate two distinct storage stages. The sloping region in the "house of cards/intercalation–adsorption" model corresponds to the Na^+ insertion between graphene layers.[68,70] The adsorption–intercalation model explains the sloping region as a result of adsorption at defects/heteroatoms.[59,95] The amorphous structure of hard carbon with defects like edge hexagonal carbon fragments and heteroatoms (O/N/H) results in many storage sites and the broad distribution of binding energy forming the voltage slope when bound to a metal ion. For the low-voltage plateau in the SIB, the models relate the plateau capacity as intercalation between graphene layers within the micro-nanocrystallites and the pore-filling/pseudo-metal cluster plating process. The elaborate study of storage mechanisms in hard carbon by surface analysis is significantly challenging. A more agreed on view is that the Na ions are hard to intercalate between graphene layers to produce a voltage plateau below 0.1 V.[96] Thus, the plateau capacity results from pore-filling/pseudo-metal cluster plating, and the associated low voltage plateau can be explained by the weak binding energy between the filled Na-ions and carbon atoms in the micropores.

In the case of K ions, the low voltage plateau shifts to 0.25 V, showing a different storage property of K ions (Fig. 5b). The pore size of hard carbon is 0.5 nm, which is smaller than the spacing of potassium-intercalated graphite (0.53 nm). Therefore, when K ions are inserted into micropores, strong coordination occurs between the K-ions and C atoms, making the insertion similar to the intercalation of potassium into graphite.[94]

The kinetics of Na/K-ion insertion by GITT shows a similar equilibrium voltage profile with similar voltage shapes obtained by the constant current test. The voltage hysteresis observed is considerably low in the case of Na and K in the plateau region (Fig. 5c and d), hence showing a different storage behavior in the plateau region from that in the sloping region. A Larger ionic radius results in a smaller hysteresis of Na and K than Li due to weaker chemical interactions with

defects/heteroatoms. The disappearing low voltage plateau in LIB results in adsorption at heteroatoms and defective structures. However, in the case of Na and K storage, a more significant fraction of capacity comes from pore filling. The intercalation capability of K-ions into graphite makes it challenging to differentiate between the insertion of K between graphene layers and local crystallites. The overall understanding of the charge-storage mechanism of HCs in SIBs and KIBs is summarized in Fig. 5e.

Tailoring the spherical morphology of carbon can have a significant effect on performance. Carbon precursors like phenol-formaldehyde (PF) resins have a significantly slow cross-linking rate of carbon. A straightforward synthesis would require the cross-linking rate and self-assembly of carbon precursor and the enhanced interaction with a soft template to compete for the carbon precursor's polymerization rate. The use of an acidic medium facilitates stronger coulombic and hydrogen bonding interactions between PF resin precursors and amphiphilic block copolymers.[97] Resorcinol has a higher polymerization rate with formaldehyde than phenol; therefore, confining the polymerization rate can be crucial for controlling the morphology. In the ''aqueous self-assembly route,'' ethanol can slow down the polymerization of the resorcinol/formaldehyde (RF) precursor, optimizing the ethanol/water volume ratio and yielding carbon spheres.[98–100] In sucrose-derived HCSs, a higher sugar concentration and temperature of 180–230 °C is considered optimum for hydrothermal synthesis leading to intermediate compounds like 1,6-anhydroglucose, fural, and 1,2,4-benzenetriol through aldol condensation, esterification, decarbonylation, and aromatization. The core formed by this nucleation is rich in –OH, C_6H_5-C═O, and O═C–O– groups, which undergo polymerization with a reactive oxygen group and grow outwards to form micro-spherical particles.[101] Polyethylene and other organic precursors yield micro-spherical carbon above 600 °C.[102] Consequently, the synthesis methods and precursors for hard carbon play a crucial role in altering the hard carbon morphology and structure that subsequently affects the storage-capacity relation. Given this, significant efforts have been made towards designing high-performance HCs from various precursors and synthetic methods to maximize the capacity contribution at all three plausible storage sites, namely, defects and edges, interlayers, and the micro/nano-pores.

The spherical morphology of hard carbon is advantageous as follows. (i) It provides a better initial coulombic efficiency (ICE) as compared to HCs with a similar surface area. A few non-spherical hard carbons showed a similar surface area below 50 $m^2\ g^{-1}$ but failed to improve the (ICE) beyond 73%, however, SHCs with a similar surface area showed ICE up to 95%.[36,47] A lower surface area per unit volume for SHCs leads to less electrolyte consumption during the first cycle. This results in a superior electrode–electrolyte interface and a stable SEI formation in SHCs. Consequently, it promotes better cyclic stability and rate capability up to a current density of 5 A g^{-1} (~20C rate). Alcántara *et al.*[103] suggested that the higher ICE for spherical HCs is due to a low surface area/volume ratio and low porosity, along with the existence of free spaces between disordered carbon layers. (ii) The spherical morphology in HC delivers greater low-voltage plateau region capacity ~86% (battery-type capacity) below 0.1 V,[49,103] which is critical for the high reversible capacity of the HC anode. (iii) It leads to a better C-rate capability at higher currents, similar to the Meso Carbon Micro Beads (MCMB) in comparison to graphite in Li-ion battery anodes, where the isotropy in the crystal orientation in spherical particles provides more effective current paths than natural and artificial graphites. The advantages of SHC, in addition to C-rate capability and ICE, are that the carbon's spherical morphology ensures high tap density, a stable structure, and electrode film preparation without a preferred crystal orientation. MSHCs offer flexible design criteria for SRC or PRC, depending on the synthesis methods and carbonization temperature, thus improving the capacity contribution.[64,101,103,104]

Diverse precursors for micro-spherical hard carbons

Sucrose, glucose, biomass, and polymer/plastic-waste-based precursors are abundant and sustainable materials for producing MSHCs. They have shown their potential in SIBs and PIBs by their low surface area, high nanopore volume, better structural stability, and high capacity of more than 350 mA h g^{-1} with significant PRC contribution.[36,38,42,53] Here, we discuss the different synthesis methods for the micro-spherical hard carbon from diverse precursors and the effects on the electrochemical performance.

Sugar-based MSHCs

Sucrose is one of the most used precursors for MSHCs. The ease of synthesis involves a moderate temperature of about 160–220 °C with the subsequent high-temperature carbonization step in an inert (Ar, N_2) atmosphere. The sucrose-based monodispersed MSHCs with uniform size and smooth surface were synthesized by the hydrothermal method, followed by carbonization at 1300 °C Fig. 6a). The structural stability could allow anodes with better cyclic stability as well as improved rate performance. The HCS-1600 delivered the first discharge and charge capacity of 335 and 279 mA h g^{-1}, respectively, with ICE of 83% at 0.1 C (30 mA g^{-1}) with 53% of PRC (Fig. 6b). The rate performance showed a sudden drop in the capacity after 0.2 C due to the rapid fading of PRC (Fig. 6c), suggesting poor Na-ion adsorption–desorption kinetics in the nanopores at lower potential. The SRC and PRC contributions depend on the synthesis methods and carbonization temperatures. The PRC arises from the filling of pores and increases with the rise in carbonization temperature. In contrast, the SRC contribution decreases due to increased graphitization as higher temperatures create fewer defects. (Fig. 6d).[42] Researchers claimed that the decay in the total capacity at a high C-rate due to the rapid plateau capacity decay suggests the poor kinetic properties of Na adsorption–desorption in the nanopores (PRC) as compared to the graphene layers (SRC). Morikawa and co-workers[47]

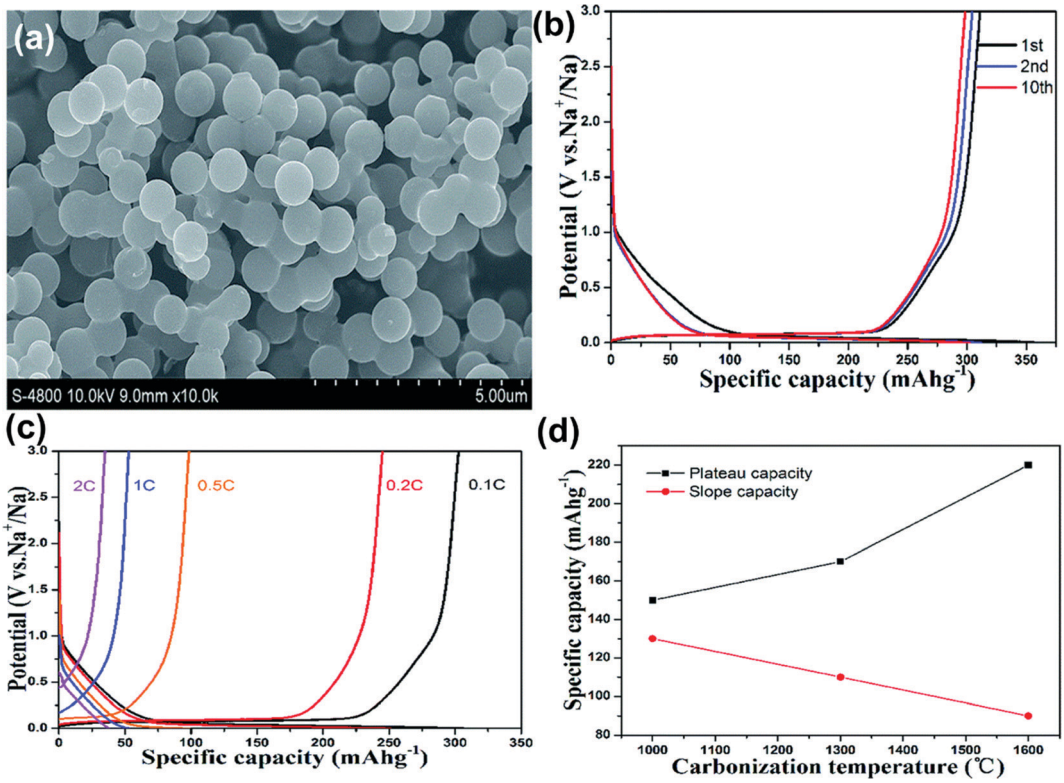

Fig. 6 (a) SEM image of HCS-1600. (b) Charge discharge curves for the 1st, 2nd, and 10th cycles of HCS-1600. (c) Rate performance test from 0.1 C to 2 C rate for HCS1600. (d) Curves showing the relation between PRC, SRC, and carbonization temperature. Reproduced with permission.[42] Copyright 2015, Royal Society of Chemistry.

developed hard carbon microspheres having diameters of 2–10 μm delivered a high capacity of 348 mA h g^{-1} at 20 mA g^{-1}. The inserted sodium–ion confined in the nanopores were revealed by small and wide-angle X-ray scattering (SAXS and WAXS), accounting for the increased capacity. The larger number of defects available in the graphene at lower temperatures promotes Na–ion adsorption at surface defects/edges, resulting in more sloping capacity contribution. SRC is influenced by the rise in carbonization temperature and the simultaneous decrease in the interlayer distances. Simultaneously, the observed larger surface area at lower synthesis temperatures can increase the number of functional groups and defects, leading to irreversible capacity loss.[105] The high defect concentration of micro-spherical HCs is directly related to poor ICE, low reversible capacity, and stability fading. During carbonization, the slow heating rate increases the number of closed pores, which improves the PRC contribution and total capacity of the carbon anode.[106] Jian and co-workers[36] reported a reversible capacity of 322 mA h g^{-1} for SIBs at 28 mA g^{-1}. T. Chen and co-workers[38] reported the synthesis of carbon microspheres using sucrose *via* the microwave-assisted solvothermal method. The increase in carbonization temperature from 300 °C to 1000 °C resulted in an increase in the carbon microspheres' surface area, leading to low ICE.[104] The best reversible capacity of 202 mA h g^{-1} at a current density of 30 mA g^{-1} was found for HCs carbonized at 500 °C due to the wider separation of graphitic layers. The differential capacity curve (dQ/dV *vs.* V) showed the SRC (above 0.2 V) and PRC (below 0.2 V) corresponding to the Na-ion nanopore filling, and the insertion of sodium ions between the graphitic layers, respectively.

The glucose-derived MSHC anode showed the capacity of 330 mA h g^{-1} at 72 mA g^{-1}, with a plateau capacity of 150 mA h g^{-1} at 0.1 V *versus* Na^+/Na.[53] The presence of latex templates provides hollow carbon spheres using glucose as the precursor at 1000 °C. The hollow spheres have a higher surface area resulting in a poor ICE, and delivered a lower charge capacity of 223 mA h g^{-1} at 50 mA g^{-1}.[46] The larger interlayer spacing of 0.401 nm accounts for the majority of the sodium storage between the graphene layers (SRC), and a capacity of ~20 mA h g^{-1} as compared to the total capacity was observed from nano-pores filling (PRC below 0.11 V).

G. Yasin *et al.*[107] fabricated MSHCs made from glucose, using the hydrothermal method (Fig. 7a and b), encapsulated with graphene oxide (G-HCS), reporting a high charge capacity of 421 mA h g^{-1} (68.45% low ICE) at a current density of 0.1 A g^{-1} as shown in Fig. 7c. The rate performance of G-HCS showed a much-improved capacity as compared to HCS and delivered 140 mA h g^{-1} at a high current density of 10 A g^{-1} for SIBs, as shown in Fig. 7d. However, MSHCs delivered a reversible capacity of 308 mA h g^{-1} at 0.1 Ag^{-1}. The maximum slope capacity for G-HCS suggests the insertion of Na-ions between

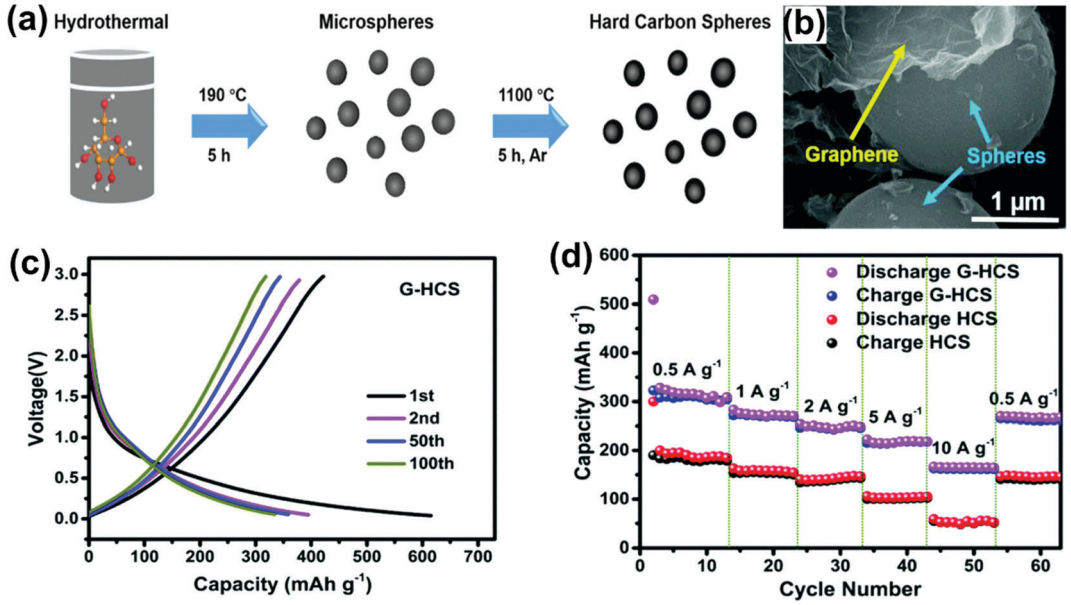

Fig. 7 (a) Schematic for the synthesis of G-HCS. (b) SEM image of G-HCS, (c) charge–discharge profile of G-HCS at 0.1 A g^{-1}, and (d) rate performance of G-HCS and HCS. Reproduced with permission.[107] Copyright 2020, Royal Society of Chemistry.

the expanded graphitic carbon layers. The G-HCS enhanced the electrolyte diffusion and kinetics of ions and electrons due to the large surface area leading to better rate capability. The larger spacing between the graphitic layer promotes excellent rate performance, having enhanced capacity at a higher current rate of 309, 272, 243, 215, and 165 mA h g^{-1} at the current densities of 0.5, 1, 2, 5, and 10 A g^{-1}, respectively.

Yang *et al.*[52] recently reported low surface area carbon microspheres by a salt-assisted hydrothermal carbonization method of glucose. NaCl played a vital role in improving the carbon conversion efficiency, microsphere size, and a more disordered structure, enhancing the specific capacity of 350 mA h g^{-1}, with a PRC of 63.8% below 0.2 V, and excellent retention of 93.4% after 200 cycles, as compared to the capacity of the sample without NaCl (323 mA h g^{-1}) at 100 mA g^{-1}. The low surface area promotes less irreversible loss, resulting in a much better ICE of 81.3%. The larger lateral width (L_a) of the graphitic domain leads to a more ordered structure, causing less accessibility to Na–ion storage sites and low PRC results. Also, the fading of the PRC at higher current density is due to poor Na–ion kinetics at a lower voltage. The sodium molybdate dihydrate ($Na_2MoO_4{\cdot}2H_2O$) precursor was synthesized *via* hydrothermal carbonization at 800 °C and resulted in porous carbon spheres (PCS) as shown in Fig. 8a.[108] The addition of molybdate dihydrate increased the surface area and pore diameter, and more micropores offered more active sites to store Na–ions. The best reversible capacity of 319.2 mA h g^{-1} was observed for PCS-120 at 50 mA g^{-1} with a larger interlayer spacing and a high surface area, leading to a sizeable irreversible capacity (Fig. 8b). The mechanism model has three voltage ranges: the first is the slope due to capacitive behavior on the surface and edge (above 1. 0 V), the second is SRC due to the adsorption/intercalation of Na–ions on and between the graphene layers (below 1.0 V), the third is PRC due to the adsorption/intercalation of the ion into the nanopores (near 5 mV). The rate performance with better retention of PCS electrodes was 2.5 times higher than CS electrodes, as shown in Fig. 8c.

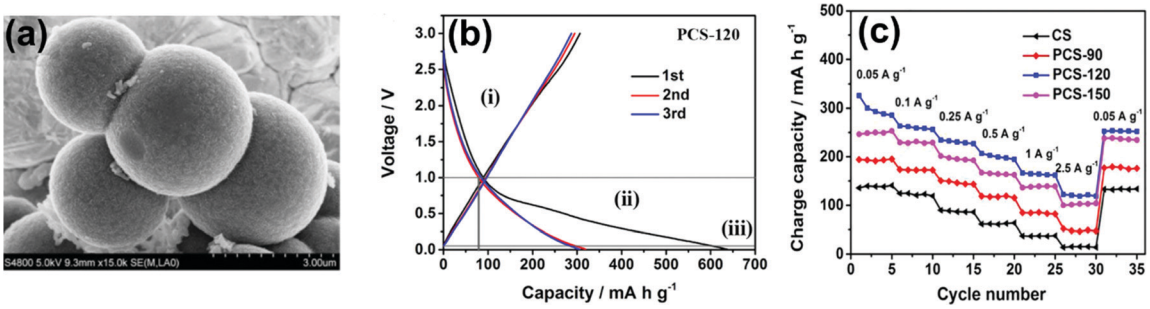

Fig. 8 (a) SEM image of PCS-120, (b) charge–discharge profile for PCS-120, and (c) rate performances for different spherical carbons at 0.05 A g^{-1} to 2.5 A g^{-1}. Reproduced with permission.[108] Copyright 2017, Elsevier.

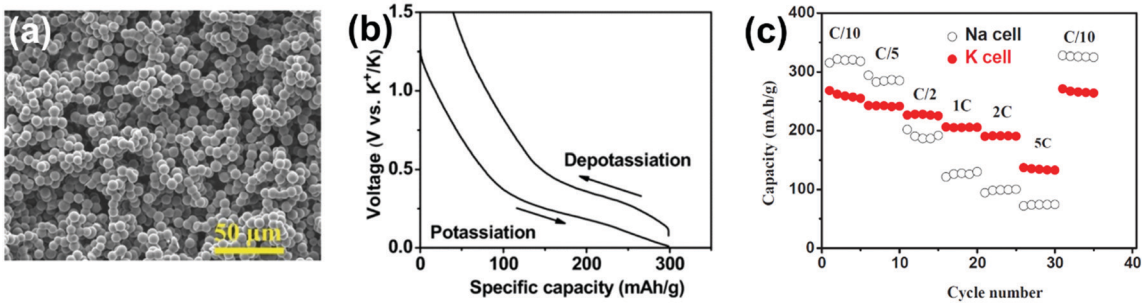

Fig. 9 (a) SEM image, (b) charge–discharge profile of PIBs, and (c) rate performances of PIBs and SIBs. Reproduced with permission.[36] Copyright 2017, Wiley.

In PIBs, the hard carbon with micro-spherical architecture also plays a crucial role in increasing the rate capability, capacity retention, and initial coulombic efficiency with an improved potassium adsorption capability.[83,85,92,109,110] However, hard and soft carbons with different morphologies are limited by the sizeable irreversible loss and low capacity retention in PIBs.[111,112] Zelang and co-workers[36] reported the micro-spherical hard carbon from glucose (Fig. 9a) *via* the hydrothermal method. It achieved a high ICE of 61.8% and reversible capacity of 262 mA h g^{-1}, with 83% capacity retention after 100 cycles at a current density of 28 mA g^{-1}, as shown in Fig. 9b. However, PIBs showed better capacity and retention than SIBs at higher current rates, as shown in Fig. 9c.

The higher potassiation voltage avoids metal plating (dendrite formation) and exhibits better rate capability and retention. Further, this group[113] reported sucrose as a precursor for micro-spherical hard carbon by a hydrothermal reaction followed by pyrolysis at 1100 °C. Using the 0.8 M KPF_6 salt in EC and DEC (1 : 1 by volume) solvent, the half-cell exhibited the reversible capacity of 260 mA h g^{-1} with an ICE of 76% at a 0.1 C rate. The excellent cycling performances at 0.2C and 1C rates are due to the unique nongraphitic structure with more disorder. The HR-TEM image confirmed the short turbostratic nanodomain before and after potassiation and the minor structural change in the hard carbon resulted in better cycling performance.

Biomass-based MSHCs

Biomass and its waste products are abundant, low-cost, and have a high carbon and low oxygen and hydrogen content to suit hard carbon anode materials. Hard carbon can pursue the biomass precursor's natural morphology based on synthesis strategies such as simple direct pyrolysis,[114,115] hydrothermal carbonizations,[106] and physical and chemical activation[116,117] processes. Biomass-based porous carbon has drawn significant attention as the anode material in LIBs, lithium–sulfur batteries (LSBs), and supercapacitors.[118–120]

Different waste biomasses with various binder components, *i.e.*, lignin, hemicellulose, or pectin, have been investigated as precursors for the synthesis of hard carbons. In particular, peanut shells and corncobs, respectively, containing lignin and hemicellulose, were successfully transformed into hard carbons. Their characteristics and electrochemical performance have been compared with those of apple (pectin)-derived hard carbon. The acid treatment has been identified as an essential step in the synthesis, as the various binder components have different sensitivities towards hydrolysis, which strongly affects the characteristics of the derived hard carbons. The various biomass compositions and structures crucially influence the process yield, surface area, elemental composition (bulk and surface), structural disorder, and impurity content of the resulting hard carbons. However, the practical application of biomass-derived carbon is limited by their relatively rare storage sites and low diffusion kinetics.[121] In sucrose and glucose, it is converted into uniform spherical hard carbon *via* hydrothermal treatment at 160 °C. At the same time, cellulose and rye straws are resistant to low-temperature hydrothermal treatment due to their intact fiber structures, and do not undergo any structural disruption. However, at a higher temperature (>220 °C), its fibrous network is disrupted, leading to the formation of micro/nano-sized cellulose fragments and spherical particles of varying sizes, confirming that synthesis methods and heat treatment play a vital role in controlling the size and structure of spherical hard carbon.[121–123] The biomass-based HC with its inherent morphology and porous structure, along with the sustainable nature of precursors, make them potential anode materials for SIBs and PIBs[100,105,113]

The carbon microspheres using the sol–gel process were achieved by C. Chen's group[124] using seafood waste chitin as a precursor, after carbonization at 800 °C. The reversible capacities of 200 mA h g^{-1} and 105 mA h g^{-1} were observed at low and very high current densities of 33.6 mA g^{-1} and 8.96 A g^{-1}, respectively. According to the relationship between current (i) and sweep rate (v), $i = av^b$, b-value was used to identify the nature of charge storage. The b-value of 0.5 represents the diffusion process, whereas 1 indicates the capacitive-dominated process. For the sodium half-cell of porous carbon microspheres, the high b-value of 0.94 shows the charge storage from greater surface adsorption of sodium ions. R. R Gaddam and co-workers reported a flame deposition method[50] to obtain MSHC of 40–50 nm from coconut oil. This biomass-derived MSHC delivered the reversible capacity of 277 mA h g^{-1} at a current density of 100 mA g^{-1} with a capacity retention of

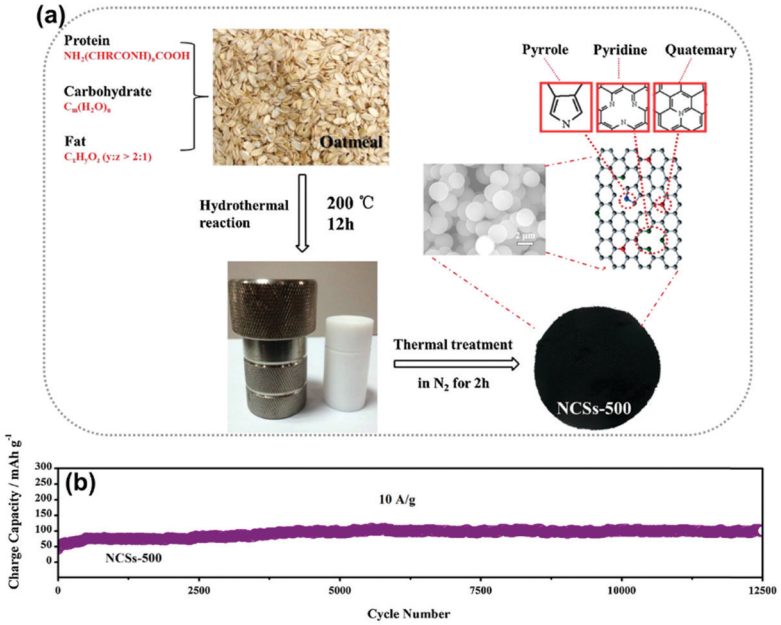

Fig. 10 (a) Schematic showing the synthesis of MSHCs using oatmeal as a carbon precursor, and (b) the long-time cyclic performance of MSHCs at 10 A g^{-1} for 12500 cycles. Reproduced with permission.[55] Copyright 2017, Elsevier.

78.3% after 20 cycles. The CV curve in the voltage range of 5 mV to 3 V shows a precise rectangular shape of a pure capacitive storage mechanism. Oatmeal,[55] having abundant C, N, and O, gave carbon microspheres by the hydrothermal–carbonization process, as illustrated in Fig. 10a. The greater surface area and larger interlayer spacing at 500 °C promoted better charge transferability, ultra-fast charging/discharging ability, and Na-ions insertion between the layers. The excellent capacity retention of 104 mA h g^{-1} was achieved after 12 500 cycles at a higher current density of 10 A g^{-1}, as shown in Fig. 10b. Rape pollen grains (RPGs)[125] were used to synthesize 3D hollow reticulate MSHCs by the pyrolysis of RPGs' hydrothermal product. The interconnected hollow carbon sphere showed type-I/IV behaviors with pore volumes ranging from 2 nm to 15 nm, and larger interlayer spacing allowed for excellent Na–ion storage. The specific discharge capacity of 145 mA h g^{-1} at a current density of 50 mA g^{-1} showed 90% capacity retention after 1000 cycles with 79% of the capacity above 0.1 V, suggesting an adsorption charge-storage process. Yeast-derived MSHCs, obtained through the hydrothermal method followed by a sulfuration procedure, were achieved by Lian *et al.*[126] The yeast cell acts both as a carbon template and the source of heteroatoms (N, P). The MSHCs exhibited excellent long cyclic stability but suffered from an insufficient reversible capacity of ~150 mA h g^{-1} at 100 mA g^{-1}. Recently, an efficient solvothermal stabilization method was reported to synthesize MSHCs from a wheat starch precursor and promoted the carbon yield.[127] MSHCs carbonized at 1100 °C exhibited an excellent reversible capacity of 320 mA h g^{-1} at a current density of 30 mA g^{-1} with enhanced ICE of 85.2%. Also, superior cycling stability at 0.4C rate delivered capacity retention of 93.2% after 300 cycles. For MSHCs with carbonization temperatures ranging from 900 to 1700 °C, the SRC decreased from 176 to 112 mA h g^{-1}, while the PRC first increased from 80 to 186 mA h g^{-1} (until the carbonization temperature of 1300 °C), and then started to decrease. The temperature-dependent defects, interlayer spacing, and graphitic domains led to such an observation.

In PIBs, Chen *et al.*[124] developed the nitrogen-rich Microspherical hard carbon from a chitin source by a sol–gel method, as illustrated in Fig. 11a. As confirmed by the SEM image (Fig. 11b), the hierarchically porous microspheres were obtained with a pore size of approximately 10 μm and a surface area of 563 m^2 g^{-1}. The high-magnification SEM (Fig. 11c) and TEM images (Fig. 11d) of the MSHC show a cross-linked hierarchically porous microsphere. The N-doped MSHC delivered the reversible capacity of ~250 mA h g^{-1} at the current density of 0.12 C (1C = 280 mA h g^{-1}) and showed an excellent capacity of 156 mA h g^{-1} at 18 C for a half cell as shown in Fig. 11e and f. Surprisingly, the same ultra-high capacity was obtained when the C-rate was increased from 18 C to 72 C. The N-doped MSHC showed no capacity decay even after 4000 cycles. In contrast, for NIBs, 200 mA h g^{-1} of reversible capacity was obtained at 0.12 C and 105 mA h g^{-1} at 36 C, which is comparatively lower than for PIBs. Yingli Zhang *et al.*[128] reported corn silk-derived carbon with protrusions and a nanosphere morphology at its surface. The N, O-enriched MSHC anode carbon delivered the initial capacity of 309.8 mA h g^{-1} and retained 82.1% of its initial capacity after 200 cycles at 0.1 A g^{-1}. An excellent capacity of 131 mA h g^{-1} was observed at 10 A g^{-1} through surface adsorption storage showing fast kinetics.

Organic polymer-based MSHCs

Hard carbons from organic polymer-based precursors mainly belong to organic resin precursors like polyacrylonitrile

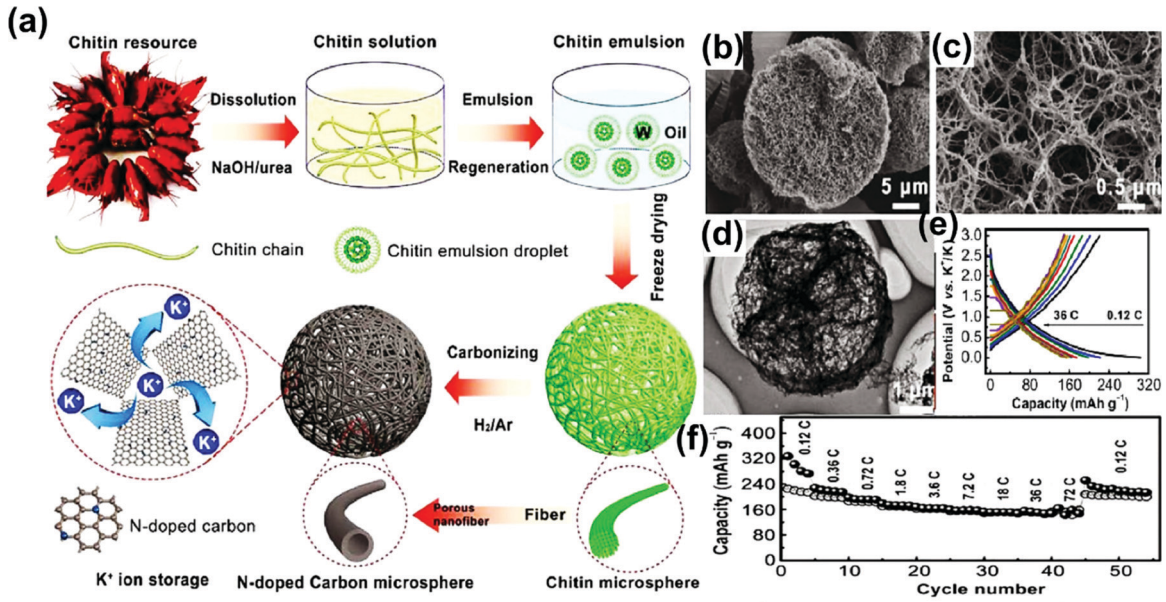

Fig. 11 (a) Schematic of the SHC synthesis from biomass waste chitin. (b and c) HR-SEM, and (d) TEM images of SHC revealing the morphology. (e) Charge–discharge curves at different current densities, and (f) the rate performances at various C-rates of biomass waste chitin. Reproduced with permission.[124] Copyright 2017, Elsevier.

(PAN),[129] phenolic resin,[44] epoxy resin,[130] and conducting organic polymers such as polyaniline (PANI).[131] Among these, the resorcinol formaldehyde resin (RF-resin) is an excellent precursor due to the ease of synthesis, availability, and high carbon yield. RF-resin is a thermosetting resin and forms a 3D network with more crosslinked structures after thermal treatment. The 3D network architecture can enhance the long cycle stability of the batteries during charge and discharge processes. It makes the resinous precursors (RF and phenolic) an excellent choice for hard carbon anodes in SIBs and PIBs.[44,49,64]

The resorcinol formaldehyde (RF) resin as a precursor for MSHCs *via* a hydrothermal controlled pyrolysis process was reported by Yu Jin *et al.*[64] The HC delivered a maximum reversible capacity of 310 mA h g^{-1} with the outstanding capacity retention of ~96.7% after 100 cycles at a current density of 20 mA g^{-1}. The larger interlayer spacing and nanopores at higher pyrolysis temperatures provide insight into the high capacity storage mechanism based on three storage sites: (1) sodium–ion storage at defective sites, called adsorption capacity (AC); (2) sodium–ion insertion into the graphene sheets, called intercalation capacity (IC); (3) sodium–ion filling into the confined spaces, called filling pore capacity (FPC). The SRC contribution due to AC gradually decreases with temperature because of fewer defects at higher carbonization temperatures. As the temperature increases to 1300 °C, PRC (IC + FPC) increases and decreases due to more graphitization. The galvanostatic intermittent titration technique (GITT) used for the Na^+ diffusion coefficient (DC) in the sodiation/desodiation curve indicates the voltage range (0–2.5 V) of the discharge curve for the three-phase model, AC (1.0–0.1 V), IC (0.1–0.03 V), and FPC (0.03–0 V). H Wang and co-workers[44] synthesized low surface area micro-spherical HCs using phenolic resin and carbonized them at higher temperatures from 800 °C to 1500 °C. At the current density of 20 mA g^{-1}, the reversible capacity first increased to 311 mA h g^{-1} at 1250 °C due to the large graphene interlayer space suitable for sodium–ion insertion decreasing because of graphitization. Qiliang Wei and co-workers[56] developed highly ordered microporous carbon (MPC) nanospheres *via* a hydrothermal method based on a soft-template (tri-block copolymer Pluronic F127) at 700 °C. At 100 mA g^{-1}, MPC-700 delivered the first specific charge capacity of 237 mA h g^{-1} (ICE = 51%) with a capacity retention of ~76% after 200 cycles. The MSHCs, through the polymerization process, using the mixture of resorcinol and formaldehyde, provided quite a low surface area of 3 m^2 g^{-1}. The presence of closed pores plays a significant role in reducing the irreversible capacity resulting in better ICE of 70% and allowing extraordinary contribution from PRC (247 mA h g^{-1} below 0.2 V) of the total reversible capacity (285 mA h g^{-1}) corresponding to sodium's insertion into the nanocavities.[103] Q. Zhang and co-workers[49] adopted spray-drying and carbonization techniques to fabricate MSHCs (RFHC) with larger graphene interlayer spacing from a resorcinol-formaldehyde resin precursor at different carbonization temperatures (T = 900 °C, 1100 °C, 1300 °C, 1500 °C), (Fig. 12a and b). The sample carbonized at 1100 °C delivered the highest reversible capacity of 321 mA h g^{-1}, having a great contribution from the plateau at a current density of 25 mA g^{-1}, with 82% ICE as shown in Fig. 12c. Interestingly, at current density of 250 mA g^{-1}, the PRC contribution almost vanished, suggesting a defect-assisted sodiation/desodiation process rather than insertion between graphene layers. Fig. 12d shows the contribution of the SRC and PRC above 0.1 V and below 0.1 V, respectively, suggesting a greater SRC for a sample at lower carbonization temperature,

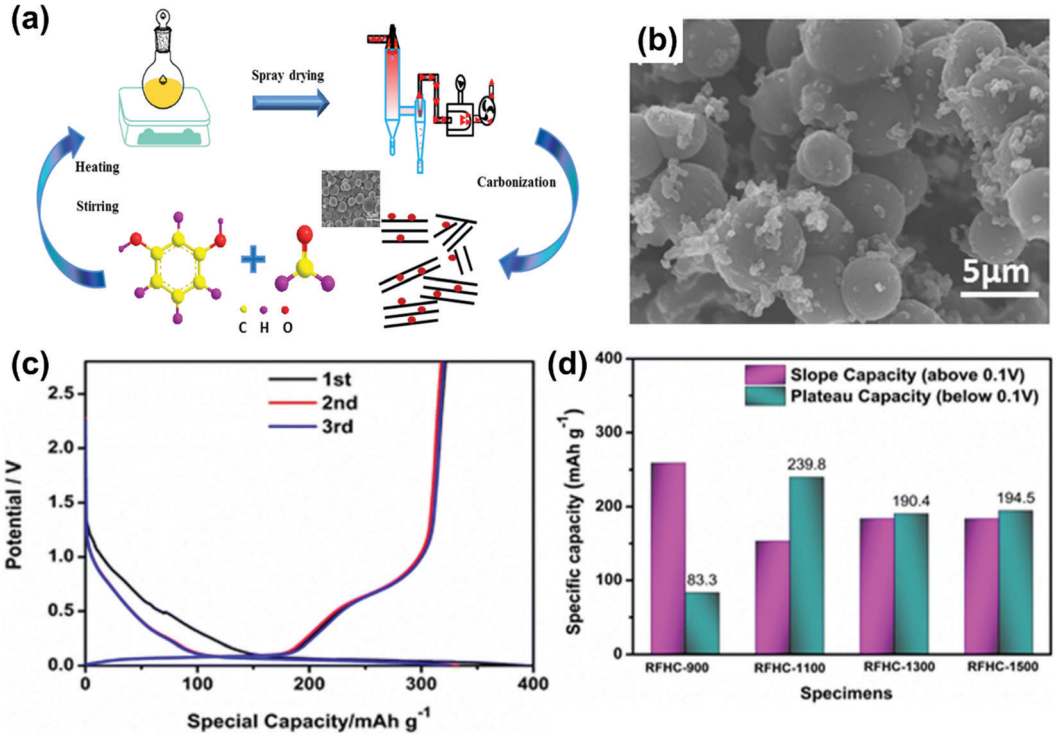

Fig. 12 (a) Synthesis pathway for micro-spherical hard carbon by the spray drying process. (b) SEM image of RFHC-1100. (c) Charge–discharge profile of RFHC-1100. (d) Capacity contribution of PRC and SRC in the first discharge charge process for voltages above and below 0.1 V. Reproduced with permission.[49] Copyright 2020, Springer.

while a maximum PRC was found for the 1300 °C sample. The synthesis of MSHC interconnected by carbon nanotubes (CNTs) using 3-aminophenol formaldehyde resin was done by L Suo *et al.*[132] to improve the electrical conductivity for better capacity and rate performance. The specific capacity of 200.6 mA h g^{-1} was observed at 100 mA g^{-1} for HCSs-CNT, which was higher than the capacity (~95 mA h g^{-1}) of simple HCSs. The incorporation of CNTs confirmed that the efficient electron kinetics and electrolyte infiltration resulted in greater capacity and higher rate capacity as compared to pristine HCs. At the current density of 1000 mA g^{-1}, HCSs and HCSs-CNTs delivered stable capacities of 49.9 mA h g^{-1} and 95.1 mA h g^{-1}, respectively, after 500 cycles.

In PIBs, S Wang *et al.*[133] developed a uniform carbon microsphere with an average diameter of 300 nm from a phenolic resin precursor. The larger lateral width (L_a) of the graphitic domain played a significant role in improving the potassium storage capacity and achieved the reversible capacity of 241 mA h g^{-1} at a current density of 25 mA g^{-1}. Recently, Zhang *et al.*[134] synthesized nano-sized porous carbon spheres (NPCS) using resorcinol *via* a simple sol–gel method as shown in Fig. 13a. The as-prepared electrode delivered a capacity of 232.6 mA h g^{-1} over 100 cycles at 200 mA g^{-1} with the KFSI-DME electrolyte system that efficiently increased the ICE to 68.2%, as illustrated in Fig. 13b. The particle size decreased to improve the contact between the electrode and electrolytes, increasing the carbon electrode's reversible capacity. The discharge capacities of SPCS at current densities of 50, 100, 200, 500, and 1000 mA g^{-1} were 345.5, 271.9, 233.2, 194.9, and 171.3 mA h g^{-1}, respectively, better than SCS and CS as shown in Fig. 13c. Some researchers realized that lower ICE values are due to the thicker SEI layer.[135] The carbon electrode performance in ether-based solvent showed better ICE as compared to ester-based solvent. Many decomposed organic products in EC/DEC formed a thick SEI layer compared to diglyme's stable, thin, and uniform SEI.[136] MSHCs using different controlled synthesis methods and precursors have shown high reversible capacity, excellent rate performance, and long stability.[30,31,77]

Heteroatom-doped/co-doped MSHCs

Heteroatom doping significantly impacts sodium storage properties due to changes in the microstructures of carbon spheres. The doping approaches have positive effects on the performance of SIBs by (1) introducing more defect sites, (2) increasing the interlayer spacing, (3) increasing the nanovoid volume, and (4) improving the electric conductivity.[137,138] Carbon doping with different heteroatoms such as N, S, P, B, O, and F has been investigated for anode materials for SIBs and PIBs.[139–142] A wider interlayer spacing and more defects contribute to the increased storage capacity through the insertion mechanism. The defect sites generated in the MSHCs structure helps to improve the electrode–electrolyte interface.[31,143] The doping of MSHCs with functional groups could promote greater capacitive performance through a pore-filling mechanism.[59]

The incorporation of N leads to a unique structure and creates defect sites, resulting in a greater capacitive contribution.

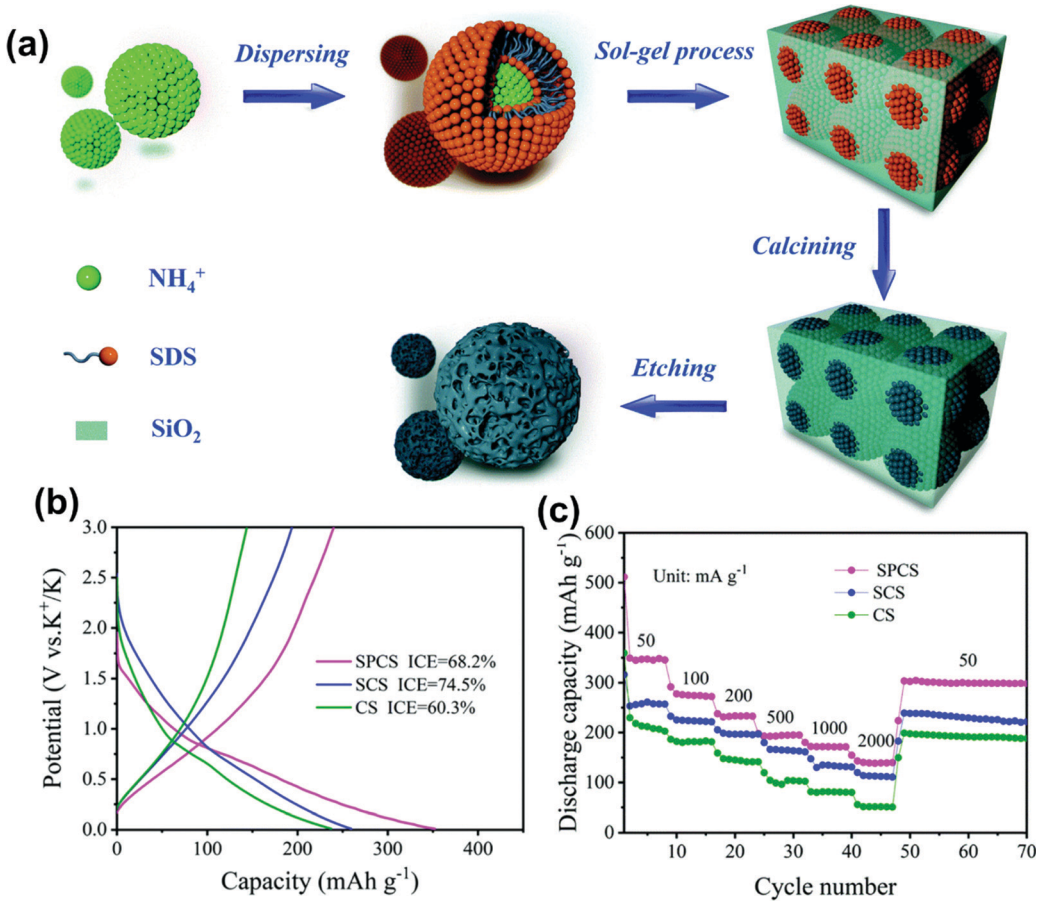

Fig. 13 (a) Schematic for the synthesis of nano-sized porous spherical carbon using the sol–gel method; (b) charge–discharge profile of NPCS, and (c) rate performance of NSCS. Reproduced with permission.[134] Copyright 2020, Royal Society of Chemistry.

Zhong *et al.*[144] reported that the N-doped mesoporous carbon spheres by hydrothermal and thermal pyrolysis using glucose and melamine delivered an excellent sodium capacity of 334.7 mA h g^{-1} and 93.9 mA h g^{-1} at a current density of 50 mA g^{-1} and 5 A g^{-1}, respectively. The material delivered a poor ICE of 23.3% due to enhanced surface reactions. The *in situ* Raman characterization suggested Na-ion adsorption above 0.3 V (SRC) and adsorption intercalation of Na-ions between 0.3–0.02 V (SRC). Agarwal *et al.*[145] reported a hydrothermal process for the N-doped nanocarbon spheres (NNCS) using sucrose as a carbon precursor. The higher surface area and more defects of NNCS provide better battery performance than the undoped nanocarbon sphere. A well developed template-assisted method for N-doped porous carbon spheres was reported by Dongdong *et al.*[146] The porous structure is critical for better cycle stability and rate performance, and delivered the high reversible capacities of 237, 215, 184, and 155 mA h g^{-1} at current densities of 0.1, 0.2, 0.5, and 1 A g^{-1}, respectively, with a capacity retention of ~67% at 0.2 A g^{-1} after 600 cycles. Xu *et al.*[43] recently fabricated porous carbon microspheres with heteroatom doping to enhance more active sites for storage. N-doped porous microspheres allowed more open pores and high surface area with a more significant graphitic layer separation, significantly enhancing the Na-ion storage capacity and delivering a high reversible capacity of 256 mA h g^{-1} at 1 A g^{-1}. It showed excellent reversible capacity retention of 291.8 mA h g^{-1} after 100 cycles at 200 mA g^{-1}.

Sulfur-doped carbon spheres significantly promoted a considerable number of active sites on the surface. The S-doped micro/mesopore carbon spheres *via* a resorcinol-formaldehyde sol–gel as a carbon precursor were presented by H. Tang *et al.*[147] A high reversible capacity of 679 mA h g^{-1} at 50 mAg^{-1} with a retention capacity of 443.4 mA h g^{-1} was achieved after 50 cycles. The S and N co-doped porous hollow carbon spheres were developed using resorcinol at 600 °C by Ye's group.[148] N-doping supports the modification of the surface electronic distribution; however, S-doping expands the graphitic interlayer distance in carbon spheres. The electrode's hierarchical structure delivered the charge capacity of 250 mA h g^{-1} at 100 mA g^{-1}, with an excellent rate performance of 185 and 140 mA h g^{-1} at 500 and 5000 mA g^{-1}. The nitrogen and oxygen co-doped carbon sphere using corn stalks *via* the hydrothermal method promotes a highly porous carbon structure with a large interlayer gap of 0.377 nm, as shown in Fig. 14a–b. Fig. 14c illustrates the specific charge capacity of 374 mA h g^{-1} with poor ICE.[149] So, achieving a higher ICE is still challenging for initial cycles. A higher surface area (more porous) promoted greater adsorption of ions, resulting in better performance at a higher current rate, and showed the reversible

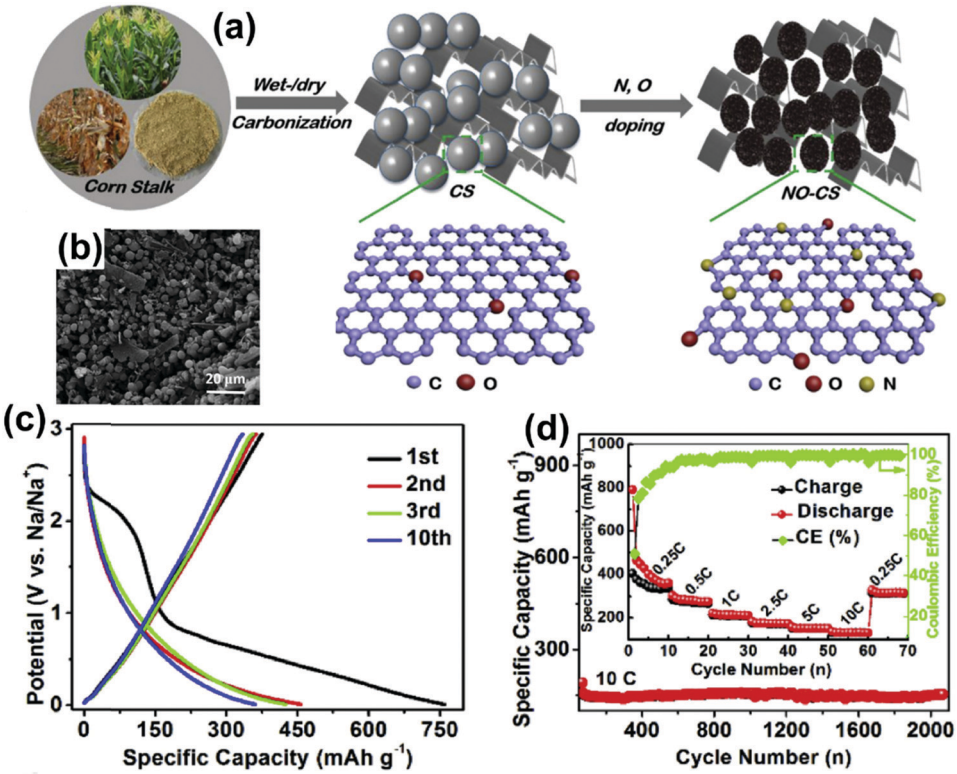

Fig. 14 (a) Synthesis pathway of N and O-doped hard carbon, (b) SEM image of N, O co-doped HC, (c) charge-discharge profile at 50 mAg^{-1}, and (d) rate performance and long-term cyclic performance at 10C rate. Reproduced with permission.[149] Copyright 2019, Elsevier.

capacity retention of 108 mA h g^{-1} after 3500 cycles at 5000 mA g^{-1}. The rate performance from 0.25C to 10C exhibited improved performance with a capacity of around 200 mA h g^{-1} at 1 C rate, and the cyclic stability at 10C rate for 2000 cycles showed excellent retention of 96.8% for long-time cycling (Fig. 14d).

Recently, carbon microspheres with B (boron), P (phosphorous), and B–P dual-doped carbon (BC, PC, and BPC) were developed by a pyrolysis method using onion salts.[150] The BPC sample (0.369 nm) had a larger interlayer spacing as compared to BC (0.342 nm), and PC (0.360 nm) facilitated more Na–ion intercalation between the graphene layer, giving more PRC regions. The reversible capacity was found to be 221.9 mA h g^{-1} for BPC (ICE = 66.6%), 126.7 mA h g^{-1} for BC (ICE = 44.6%) and 101.2 mA h g^{-1} for PC (ICE = 35.7%) at a current density of 50 mA g^{-1}.

Doped carbon spheres for PIBs have also shown improved structural stability and storage performance. C Chen *et al.*[124] reported the fabrication of nitrogen-doped micro-spherical hard carbon using chitin as a carbon precursor. At a high current rate of 72C (1 C = 280 mA g^{-1}), a reversible capacity of 154 mA h g^{-1} was observed after 4000 cycles showing extraordinary retention properties. Ruan *et al.*[151] achieved excellent reversible capacity of 241, 201, and 183 mA h g^{-1} after 100 cycles at the respective current rate of 0.05, 0.1, and 1.0 A g^{-1} for nitrogen-doped hollow carbon nanospheres prepared by dopamine. J. Ge *et al.*[152] introduced a novel zinc catalysis method for N-doped carbon microspheres (CMSs) using graphite C_3N_4 as a precursor. As shown in Fig. 15a, the micro-spherical carbons mitigate the volume expansion issue in PIBs and provide additional active sites that assist potassiation. The high reversible capacities of 328, 278, 225, 180, 164, 150, and 125 mA h g^{-1} were reported at 100, 200, 500, 1000, 1500, 2000, and 3000 mA g^{-1}, respectively as shown in Fig. 15b. Sulfur-doped carbon creates a covalent bond and nanoconfined sulfur that maximize capacity retention by lowering the irreversible loss.[153] The sulfur-rich carbon spheres exhibited a very high reversible capacity of 581 mA h g^{-1} at 25 mA g^{-1} and delivered 202, 160, and 110 mA h g^{-1} at current rates of 1.5, 3, 5 A g^{-1}, respectively. Chen and co-workers[154] developed high surface area porous hard carbon microspheres by sulfur and oxygen co-doping. High surface defects with better structure stability promoted a high reversible capacity of 230 mA h g^{-1} and high capacity retention of 226.6 mA h g^{-1} after 500 cycles at the current density of 50 mA g^{-1}. The results confirmed that in PIBs, HCMSs can deliver high energy density batteries with better retention and high rate performance.

Plastic waste-based MSHCs

The cost-effective recycling of increasing amounts of non-biodegradable plastic waste into a valuable product is crucial for environmental sustainability. The plastic waste precursors include polyethylene terephthalate (PET), polyvinyl chloride (PVC), high and low-density polyethylene (HDPE and LDPE), polypropylene (PP), polystyrene (PS), polycarbonate (PC), and nylon. They generate hierarchical micro-spherical carbons for application in the field of batteries and supercapacitors.[155–157]

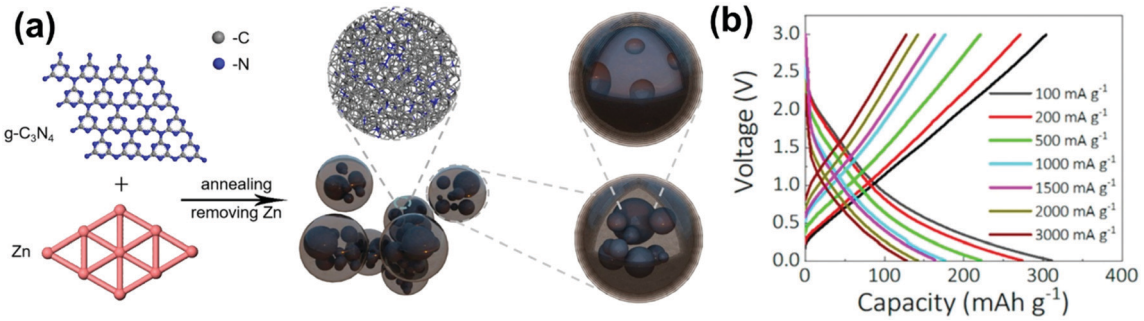

Fig. 15 (a) Scheme for the Zn-catalyzed process for carbon microspheres (CMSs) and (b) rate performance charge–discharge curve. Reprinted (adapted) with permission.[152] Copyright 2020, American Chemical Society.

Here, we focus on synthesizing micro-spherical hard carbon from plastic waste as a precursor for battery applications.

Pol *et al.*[158] reported polyethylene-based plastic waste to fabricate spherical carbon particles (SCPs) by an autogenic reaction (Fig. 16a). At a current density of 23.5 mA g^{-1}, SCPs/Li cells generated the reversible capacity of 227 mA h g^{-1} with 60% of the initial irreversible capacity loss and showed stable cycling performance and a discharge capacity of 237 mA h g^{-1} after 200 cycles as shown in Fig. 16(b and c). Due to improved graphitic order, the irreversible loss was reduced from 60% to 20% in high-temperature SCPs/Li cells. Kali *et al.*[57] fabricated micro-spherical carbon using the waste from a bicycle rubber tube by a controlled oxidation process. This trash to treasure electrode for the Li half-cell delivered the first charge capacity of 267.09 mA h g^{-1} with 31.9% ICE at a current density of 100 mA g^{-1}. The better structure stability maintained the reversible capacity of ~190 mA h g^{-1} after 1000 cycles at the current rate of 2C (~1.339 mA).

In SIBs application, Pol *et al.*[58] achieved carbon spheres using mesitylene (or LDPE bags) *via* the same autogenic process at 700 °C. The interlayer spacing of ~ 0.34 nm close to 0.335 nm of graphite suggests graphene-like properties. The inadequate capacity of ~ 125 mA h g^{-1} was seen for micro-spherical carbon at the current density of 30 mA g^{-1}, which was attributed to a lack of sodium ion pore-filling, whereas hard carbon showed better reversible capacity (Fig. 16d and e). However, micro-spherical carbon had high capacity and good capacity retention at high current rates due to sodiation into graphene regions, as illustrated in Fig. 16f. Apart from micro-spherical carbon, plastic waste conversion into activated carbon can also play a promising role as a negative electrode in LIBs, SIBs, and PIBs due to its highly porous structure. Uttam's research group[159] converted the electronic waste plastic into porous activated carbon *via* a fast and slow heat-treatment process. The sample carbonized at 700 °C delivered a specific capacity of 190 mA h g^{-1} after 25 cycles at a low current density

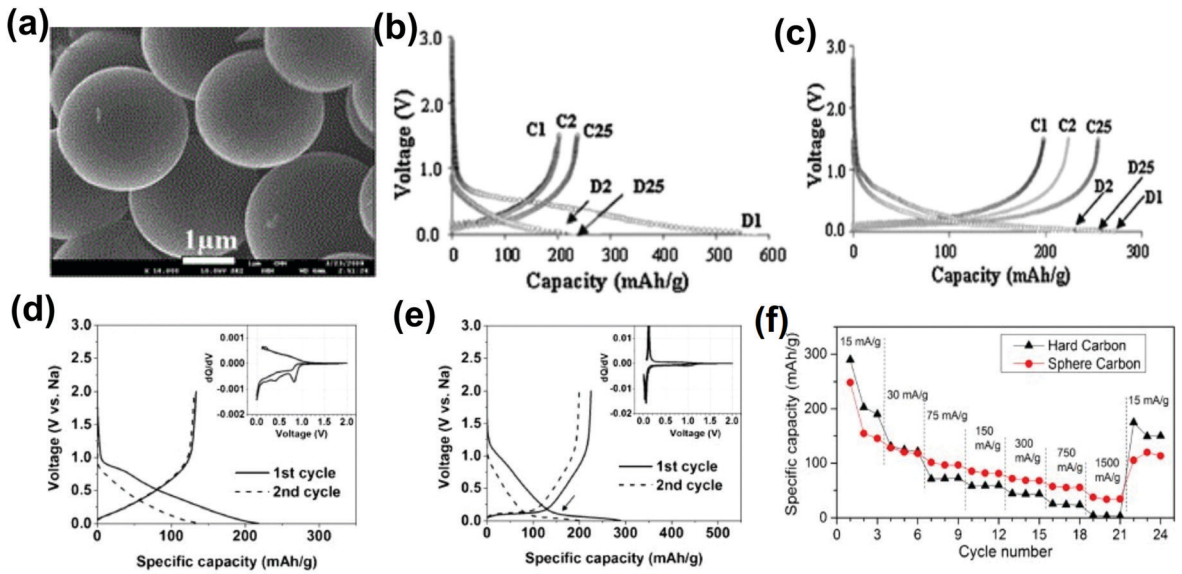

Fig. 16 (a) SEM image of LDPE-derived carbon spheres. Charge–discharge profile of spherical carbon *vs.* Li/Li^+ calcined at (b) 700 °C, (c) 2400 °C. Reproduced with permission.[158] Copyright 2011, Royal Society of Chemistry. Charge–discharge curve *vs.* Na/Na^+ of (d) plastic waste-derived spherical carbon, and (e) plastic waste-derived hard carbon. (f) The rate performance of plastic waste-based carbon. Reproduced with permission.[58] Copyright 2014, Elsevier.

Table 1 Summary of micro-spherical hard carbons from diverse precursors as anodes for SIBs

Precursor (methods)	CT (°C)	Electrolyte	*V*	Specific capacity (mA h g^{-1})	ICE (%)	Cyclability (mA h g^{-1})	Rate performance (mA h g^{-1})	Ref.
Sucrose (hydrothermal)	1600	1 M $NaClO_4$ in EC:PC	0–3 V	*310 @ 30 mA g^{-1}	83	290 after 100 N @ 30 mA g^{-1}	110 @ 150 mA g^{-1}	42
Sucrose (hydrothermal)	1100	0.8 M $NaClO_4$ in EC:DEC	0.01–1.5 V	*322 @ 28 mA g^{-1}	75.7	—	190 @ 140 mA g^{-1}; 127 @ 280 mA g^{-1}; 97 @ 560 mA g^{-1}	36
Sucrose (hydrothermal)	1300	1 M $NaClO_4$ in EC:DEC	0–2 V	*361 @ 20 mA g^{-1}	86.1	94% after 100 N @ ß20 mA g^{-1}	—	106
Sucrose (hydrothermal)	1400	1 M $NaPF_6$ in EC:DEC	0–2.5 V	*348 @ 20 mA g^{-1}	95.2	—	—	47
Sucrose (microwave-assisted solvothermal)	500	1 M $NaClO_4$ in EC:PC	0.005–3 V	*202 @ 30 mA g^{-1}	—	183 after 50 N @ 30 mA g^{-1}	149 @ 100 mA g^{-1}; 80 @ 1000 mA g^{-1}	38
Sucrose (microwave assisted solvothermal)	1000	1 M $NaClO_4$ in EC:PC	0.005–1.5 V	*385 @ 30 mA g^{-1}	75.5	83% after 50N @ 30 mA g^{-1}	265 @ 300 mA g^{-1}; 100 @ 1500 mA g^{-1}	77
Glucose (hydrothermal)	1100	1 M $NaClO_4$ in EC:DEC	0.01–3 V	#421 @ 100 mA g^{-1}	—	327 after 200 N @ 100 mA g^{-1}	272 @ 1 A g^{-1}; 215 @ 5 A g^{-1}	107
Glucose (hydrothermal)	1000	1 M $NaClO_4$ in PC	0.001–3 V	#223 @ 50 mA g^{-1}	41.5	160 after 100 N @ 100 mA g^{-1}	168 @ 200 mA g^{-1}; 100 @ 2 A g^{-1}; 75 @ 5 A g^{-1}	46
Glucose (hydrothermal)	800	1 M $NaClO_4$ in EC:PC	0.005–3 V	*319.2 @ 50 mA g^{-1}	—	249.9 after 50 N @ 50 mA g^{-1}	234.5 @ 250 mA g^{-1}; 166.7 @ 1 A g^{-1}; 122.2 @ 2.5 A g^{-1}	108
Glucose with NaCl (hydrothermal	1200	1 M $NaClO_4$ in EC:DMC	0.001–3 V	*357 @ 100 mA g^{-1}	71.2	327 after 200 N @ 100 mA g^{-1}	314 @ 200 mA g^{-1}; 261 @ 0.5 A g^{-1}; 167 @ 1 A g^{-1}	52
Resorcinol formaldehyde (RF) (hydrothermal)	1300	1 M $NaClO_4$ in EC:PC	0–2 V	*310 @ 20 mA g^{-1}	84	300 after 100 N @ 20 mA g^{-1}	—	64
Resorcinol (spray drying carbonization)	1100	1 M $NaClO_4$ in EC:DEC	0–2.8 V	*321 @ 0.1 C	82	281 after 200 N @ 0.1 C	200 @ 0.4 C	49
Resorcinol (polymerization)	950	1 M $NaClO_4$ in EC:DMC	0–3 V	*285 @ 0.1 C	70	—	—	103
PVDF (direct pyrolysis)	500	1 M $NaClO_4$ in PC	0–3 V	*269 @ 50 mA g^{-1}	39.7	129 after 100 N @ 50 mA g^{-1}	140 @ 200 mA g^{-1}	139
Aminophenol formaldehyde (direct pyrolysis)	900	1 M $NaClO_4$ in EC:DEC: FEC	0.01–3 V	#200.6 @ 100 mA g^{-1}	33.1	151.7 after 100 N @ 100 mA g^{-1}	214 @ 30 mA g^{-1}; 129 @ 200 mA g^{-1}; 82 @ 2000 mA g^{-1}	132
Phenol (hydrothermal)	700	1 M $NaClO_4$ in PC	0–3 V	*230 @ 100 mA g^{-1}	51	180 after 100 N @ 100 mA g^{-1}	210 @ 200 mA g^{-1}; 132 @ 2000 mA g^{-1}	56
Phenol (hydrothermal)	1250	1 M $NaClO_4$ in EC:DMC	0.01–2.7 V	*311 @ 20 mA g^{-1}	60.2	80% after 100 N @ 20 mA g^{-1}	165 @ 100 mA g^{-1}; 78 @ 200 mA g^{-1}	44
LDPE (autoclave technique)	700	1 M $NaClO_4$ in PC	0.01–2 V	*200 @ 15 mA g^{-1}	68.9	92 after 50 N @ 150 mA g^{-1}	40 @ 1.5 A g^{-1}	58
N-doped:Sucrose (Autoclave technique)	—	1 M $NaClO_4$ in EC:DEC	0.01–2 V	#256 @ 30 mA g^{-1}	43.5	245 after 200 N @ 30 mA g^{-1}	—	145
N-doped:benzenetri carbosxylic acid (hydrothermal)	800	1 M $NaCF_3SO_3$ in DEGDME	0.01–3 V	*298 @ 200 mA g^{-1}	75.2	291.8 after 100 N @ 200 mA g^{-1}	285 @ 400 mA g^{-1}; 265 @ 800 mA g^{-1}; 256 @ 1000 mA g^{-1}	43
N-Doped:glucose & melamine (direct pyrolysis)	800	1 M $NaClO_4$ in EC:DEC	0.02–3 V	*334.7 @ 50 mA g^{-1}	25.2	228 after 300 N @ 50 mA g^{-1}	93.9 @ 5000 mA g^{-1}	144
N-Doped:oatmeal (hydothermal)	500	1 M $NaClO_4$ in EC:PC	0.005–3 V	*320 @ 50 mA g^{-1}	—	336 after 50 N @ 50 mA g^{-1}	102 @ 10 A g^{-1}	55
N & O co-doped:corn stalks (wet/dry pyrolysis)	1200	1 M $NaClO_4$ in EC:DEC	0.01–3 V	*360.7 @ 50 mA g^{-1}	49.2	270 after 200 N @ 50 mA g^{-1}	210 @ 200 mA g^{-1}; 148 @ 1000 mA g^{-1}; 130 @ 2000 mA g^{-1}	149
S-Doped: RF resin (sol gel)	600	1 M $NaClO_4$ in EC:PC	0.005–3 V	*679.3 @ 50 mA g^{-1}	—	443 after 50 N @ 50 mA g^{-1}	294.9 @ 2500 mA g^{-1}	147
N & S doped: RF resin (direct pyrolysis)	600	1 M $NaClO_4$ in EC:DEC	0.01–3 V	*250 @ 100 mA g^{-1}	27.7	180 after 200 N @ 100 mA g^{-1}	185 @ 500 mA g^{-1}; 140 @ 5 A g^{-1}	148
B & P co-doped: Onium salt (pyrolysis)	1000	1 M $NaClO_4$ in EC:DEC	0.01–3 V	—	66.6	221.9 after 200 N @ 50 mA g^{-1}	102 @ 1 A g^{-1}	150

CT: Carbonization temperature; *: first reversible capacity; #: first charge capacity; ICE: initial coulombic efficiency; N: cycle.

of 3 mA g^{-1}. They observed that with the increase in carbonization temperature from 700 to 900 °C, the PRC contribution was reduced, suggesting that Na^+ filled the nanopores and enhanced the sloping region capacity.

In contrast, Na ion's insertion between the graphene layer appeared in the low plateau region due to decreased interlayer spacing. Since this topic is new and emerging, only a few reports have discussed utilizing waste as a useful carbonaceous

Table 2 Summary of micro-spherical hard carbons from diverse precursors as anodes for PIBs

Precursors (methods)	CT (°C)	Electrolyte	*V*	Specific capacity (mA h g^{-1})	ICE (%)	Cyclability (mA h g^{-1})	Rate performance (mA h g^{-1})	Ref.
Sucrose (hydrothermal)	1100	0.8 M KPF_6 in EC: DEC	0.01–1.5	*262 @ 28 mA g^{-1}	61.8	217.46 after 100 N @ 28 mA g^{-1}	229 @ 140 mA g^{-1}, 205 @ 280 mA g^{-1}, 190 @ 560 mA g^{-1}, 136 @ 1400mA g^{-1}	36
Resorcinol (hydrothermal)	900	0.8 M KPF_6 in EC:DEC	0.01–3	*232.6 @ 200 mA g^{-1}	68.2	165.2 after 1500 N @ 1000 mA g^{-1}	165.2 @ 1000 mA g^{-1} 129.7 @ 2000 mA g^{-1}	134
Aerosol (spray-pyrolysis)	900	1.0 M KFSI in EC: DEC	0–2.5	#188.2 @ 50 mA g^{-1}	10.6	154.5 after 200 N @ 50 mA g^{-1}	170.5 @ 50 mA g^{-1}, 138.1 @ 100 mA g^{-1}, 111.6 @ 200 mA g^{-1}, 84.8 @ 500 mA g^{-1}, 69.1 @ 1000mA g^{-1}, 55 @ 2000mA g^{-1}	162
Resorcinol (routinez self -template strategy)	800	0.8 M KPF_6 in EC: DEC	0–3	#370.2 @ 200 mA g^{-1}	44.2	192.7 after 5000 N @ 200 mA g^{-1}	365.5 @ 200mA g^{-1}, 296.9 @ 400 mA g^{-1}, 247.7 @ 600 mA g^{-1}, 215.2 @ 1000 mA g^{-1}, 182.2 @ 2000 mA g^{-1}, 137.0 @ 4000 mA g^{-1}	163
3-Aminophenol (self-template strategy)	1200	0.8 M KPF_6 in EC: DEC	0.01–2	#212 @ 558 mA g^{-1}	—	201.4 after 100 N @ 558 mA g^{-1}	—	164
m-Phenylenediamine (Controlled polymerization)	1200	0.8 M KPF_6 in EC: DEC	0.01–2	#241.2 @ 28 mA g^{-1}	—	219.49 after 100 N @ 28 mA g^{-1}	—	165
S/N Doped:polypyrrole (PPy) (*In situ* doping)	800	0.8 M KPF_6 in EC: DEC	0.01–3	#460.6 @ 100 mA g^{-1}	67.7	356.3 after 150N @ 100 mA g^{-1}	228.1 @ 5000 mA g^{-1}	166
Oxygen-rich: Urea (surfactant-assisted precipitation – polymerization)	900	0.8 M KPF_6 in EC: DEC	0.01–2	*278.6 @ 27.9 mA g^{-1}	27.6	192.7 after 900N @ 27.9 mA g^{-1}	278.6 @ 27.9 mA g^{-1}, 238.7 @ 55.8 mA g^{-1}, 211.5 @ 139.5 mA g^{-1}, 191.8 @ 279 mA g^{-1}, 170.9 @ 558 mA g^{-1} 146.6 @ 1395 mA g^{-1}	167
S/O codoped: epoxy/mercaptan monomers (polymerization)	800	0.8 M KPF_6 in EC: DEC	0.01–2.5	#358.6 @ 50 mA g^{-1}	61.7	226.6 after 100 N @ 50 mA g^{-1}	230 @ 50 mA g^{-1}, 213 @ 200 mA g^{-1}, 176 @ 500 mA g^{-1}, 158 @ 1000 mA g^{-1}	154
Sulfur grafted: resorcinol (hydrothermal)	450	0.8 M KPF_6 in EC: DEC	0–3	#1112 @ 25 mA g^{-1}	51.4	581 @ 25 mA g^{-1}	202 @ 1500 mA g^{-1}, 160 @ 3000 mA g^{-1}, 110 @ 5000 mA g^{-1}	153
MoS_2 Composite: resorcinol (self-template strategy)	800	1 M KFSI in DME	0–3	#376.4 @ 500 mA g^{-1}	37.4	254.9 after 100N @ 500 mA g^{-1}	420.7 @ 50 mA g^{-1}, 367 @ 100 mA g^{-1}, 343.8 @ 200 mA g^{-1}, 243.9 @ 500 mA g^{-1}, 162.7 @ 1000 mA g^{-1}, 93.1 @ 2000 mA g^{-1}	168
Nitrogen/Oxygen doped: NH_2-MIL-101(Al)	—-	0.8 M KPF_6 in EC: DEC	0.01–3	#315 @ 50 mA g^{-1}	25	130 after 1100N @ 1050 mA g^{-1}	118 @ 3000 mA g^{-1}	90

CT: Carbonization temperature; *: first reversible capacity; #: first charge capacity; ICE: initial coulombic efficiency; N: cycle.

product.[57,58,157,159–161] The focus on carbonaceous energy materials from plastic wastes will be a sustainable, green solution for the future.

Tables 1 and 2 respectively summarize the carbonization temperature and electrochemical performances of micro-spherical hard carbons derived from various precursors as anode materials for SIBs and PIBs reported to date in the literature.

Conclusion and perspectives

This review focuses on the choice of sustainable precursors for MSHCs and their effects on the surface morphology, porosity, interlayer spacing of the graphitic layer, and confined nanopores, influencing the anodic performance of SIBs and PIBs. The sufficiently cross-linked precursors with more C content and low O, H, are suitable precursors for MSHCs and show higher electrochemical performance. Heteroatoms such as N, S, P, and solvents, which promote stronger H-bonding, allow reactants to gather into tiny emulsion droplets and aggregates to form micro-spherical hard carbons (MSHCs). The micro-spherical morphology of HCs can provide optimum surface-controlled phenomena, improve mobile ion kinetics, and enhance electronic conductivity, allowing for better electrochemical performances. Moreover, the stable microstructure of MSHCs sustaining mechanical stress generated during repeated charge/discharge cycling ensures high capacity retention, which is critical for the sustainable anode.

The MSHCs from sugar precursors like glucose and sucrose with low surface area and high nanopore volume allow easy ion accessibility for Na^+/K^+ insertion. Synthetic polymers/resins, due to their lower oxygen content, help to prepare MSHCs with a low surface area, providing higher ICE with high reversible capacity and better cyclic stability. The biomass-based and plastic-waste precursors-based MSHCs are ideal for high-energy and high-power battery anode materials and could provide greener, sustainable solutions for energy storage systems. The MSHCs obtained from biomass provide porosity, and the interlayer spacing can be tailored by adjusting the carbonization temperature. The heteroatom-doped hard carbon-based anode effectively increases the interlayer spacing with more active adsorption sites to improve the Na^+/K^+ adsorption/desorption process. It faces substantial irreversible losses in the initial cycle and low cyclic performance due to higher surface area. The inherent low and moderate surface area of MSHCs

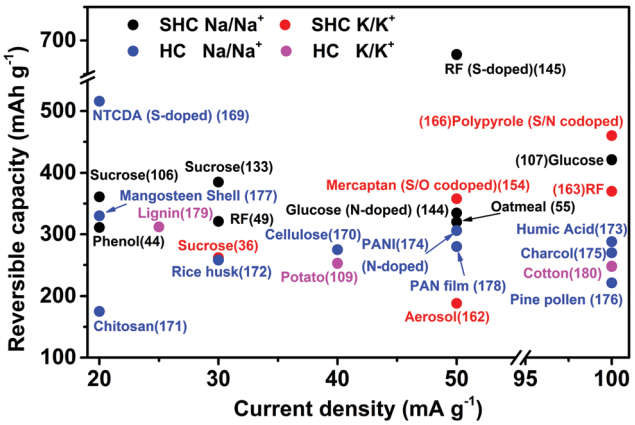

Fig. 17 A comparative overview of the micro-spherical hard carbons (MSHCs) and hard carbons (HCs) derived from diverse precursors as anodes for SIBs and PIBs.

make it more attractive over porous hard carbon with less SEI layer formation/side reactions, leading to better cyclic stability, ICE during the initial cycles, rate capability, and greater PRC contribution.

Fig. 17 shows the comparative results for MSHCs and other HCs derived from different precursors for SIBs[169–178] and PIBs.[179,180] The MSHCs show enhanced reversible capacity at higher C-rates than HCs in both non-aqueous alkali–ion batteries. The MSHCs derived from organic polymer-based resins doped with S and co-doped with S and N show the best performance as anode materials in SIBs and PIBs.

The sodium and potassium storage mechanism and capacity-storage relation in MSHCs are critical in designing a high capacity, high rate capability, and sustainable anode material. Optimized specific capacity contribution and high initial coulombic efficiency (ICE) are the needs of the hour in MSHCs. However, achieving uniform micro-spherical hard carbons with low porosity and larger interlayer graphitic spacing is challenging to accommodate sodium ions at higher rates with high plateau capacity and better ICE. The interplay of plateau capacity (PRC) and slope capacity (SRC) for Na^+/K^+ storage is critical in designing the hard carbon anode batteries. With any precursor, the increase in carbonization temperature (i) improves the structural ordering, (ii) creates fewer defects to provide a lower surface area and (iii) more confined pores, which will simultaneously enhance the PRC and ICE. The increasing degree of graphitization (decreasing interlayer spacing) with temperature influences the intercalation/deintercalation kinetics of Na^+/K^+ in hard carbons. Also, the micropores/nanopores in micro-spherical carbons exhibit enhanced PRC from the filling up of pores at low potentials. The influences of microporosity and inaccessible closed pores on the PRC at low voltages are critical in improving the Na-ion insertion and storage of the MSHCs. The aim should be to achieve maximum capacity at different C-rates for either a high energy density or fast charging anode by fine-tuning the hard carbon microstructure for specific battery applications. An ambiguous proposed Na^+/K^+ storage mechanism such as ''adsorption-intercalation'' ''intercalation pore-filling'' needs more experimental work involving ex-situ and in-situ NMR and EPR spectroscopy. Also, selecting appropriate advanced techniques and careful structure analysis is critical to understanding the storage behavior of hard carbon materials. The safety aspects of MSHCs in SIBs and PIBs, especially near the metal plating low potentials, also need to be further addressed. A full cell fabrication of the as-synthesized MSHCs in SIBs and PIBs is significant for achieving the true potentials of MSHCs as anode materials for commercialization.

Fig. 18 shows the comparative plot of best-performing MSHCs from different precursors to synthesize micro-spherical hard carbon for SIBs and PIBs. In both cases, the heteroatom-doped MSHCs achieved the highest capacity at all C-rates.

Author contributions

Nagmani: methodology, resources, figures – permission, reproduction & adaption, and writing – original draft preparation, review and editing. Ashwani Tyagi: methodology, resources, figures – permission, reproduction & adaption, and writing – original draft preparation and editing. Sreeraj Puravankara:

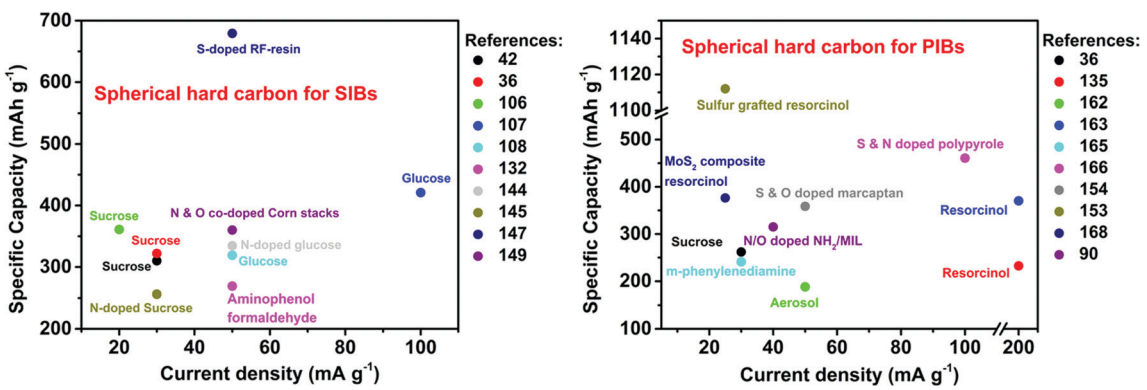

Fig. 18 Specific capacities reported in the literature to date at different C-rates for all precursor-based micro-spherical hard carbons in (a) SIBs and (b) PIBs.

conceptualization, supervision, visualization, resources, writing – review and editing, funding acquisition, and project administration.

Conflicts of interest

The authors have no conflicts to declare.

Acknowledgements

This work was supported by funding from the Ministry of Education, GoI through the IMPRINT – I grant (F. No. 3-18/2015-TS-TS.I, Dt. 29-11-2016) and Department of Science & Technology, GoI (DST/TMD/MES/2K16/77(C), Dt. 12-06-2017). Nagmani and A Tyagi acknowledge support from the Ministry of Education, GoI, and the Indian Institute of Technology Kharagpur, India, for their doctoral fellowships.

References

1 V. Palomares, P. Serras, I. Villaluenga, K. B. Hueso, J. Carretero-González and T. Rojo, Na-Ion Batteries, Recent Advances and Present Challenges to Become Low Cost Energy Storage Systems, *Energy Environ. Sci.*, 2012, **5**(3), 5884–5901, DOI: 10.1039/c2ee02781j.

2 V. Palomares, M. Casas-Cabanas, E. Castillo-Martínez, M. H. Han and T. Rojo, Update on Na-Based Battery Materials. A Growing Research Path, *Energy Environ. Sci.*, 2013, **6**(8), 2312–2337, DOI: 10.1039/c3ee41031e.

3 H. He, D. Sun, Y. Tang, H. Wang and M. Shao, Understanding and Improving the Initial Coulombic Efficiency of High-Capacity Anode Materials for Practical Sodium Ion Batteries, *Energy Storage Mater.*, 2019, **23**, 233–251, DOI: 10.1016/j.ensm.2019.05.008.

4 S. Roberts and E. Kendrick, The Re-Emergence of Sodium Ion Batteries: Testing, Processing, and Manufacturability, *Nanotechnol. Sci. Appl.*, 2018, **11**, 23–33, DOI: 10.2147/NSA.S146365.

5 M. Dahbi, T. Nakano, N. Yabuuchi, S. Fujimura, K. Chihara, K. Kubota, J. Y. Son, Y. T. Cui, H. Oji and S. Komaba, Effect of Hexafluorophosphate and Fluoroethylene Carbonate on Electrochemical Performance and the Surface Layer of Hard Carbon for Sodium-Ion Batteries, *ChemElectroChem*, 2016, **3**(11), 1856–1867, DOI: 10.1002/celc.201600365.

6 B. L. Ellis and L. F. Nazar, Sodium and Sodium-Ion Energy Storage Batteries, *Curr. Opin. Solid State Mater. Sci.*, 2012, **16**(4), 168–177, DOI: 10.1016/j.cossms.2012.04.002.

7 T. Liu, Y. Zhang, Z. Jiang, X. Zeng, J. Ji, Z. Li, X. Gao, M. Sun, Z. Lin, M. Ling, J. Zheng and C. Liang, Exploring Competitive Features of Stationary Sodium Ion Batteries for Electrochemical Energy Storage, *Energy Environ. Sci.*, 2019, **12**, 1512–1533, DOI: 10.1039/c8ee03727b.

8 J. F. Whitacre, T. Wiley, S. Shanbhag, Y. Wenzhuo, A. Mohamed, S. E. Chun, E. Weber, D. Blackwood, E. Lynch-Bell, J. Gulakowski, C. Smith and D. Humphreys, An Aqueous Electrolyte, Sodium Ion Functional, Large Format Energy Storage Device for Stationary Applications, *J. Power Sources*, 2012, **213**, 255–264, DOI: 10.1016/j.jpowsour.2012.04.018.

9 M. Á. Muñoz-Márquez, D. Saurel, J. L. Gómez-Cámer, M. Casas-Cabanas, E. Castillo-Martínez and T. Rojo, Na-Ion Batteries for Large Scale Applications: A Review on Anode Materials and Solid Electrolyte Interphase Formation, *Adv. Energy Mater.*, 2017, **7**(20), 1700463, DOI: 10.1002/aenm.201700463.

10 H. Zhang, I. Hasa and S. Passerini, Beyond Insertion for Na-Ion Batteries: Nanostructured Alloying and Conversion Anode Materials, *Adv. Energy Mater.*, 2018, **8**(17), 172582, DOI: 10.1002/aenm.201702582.

11 X. Wu, D. P. Leonard and X. Ji, Emerging Non-Aqueous Potassium-Ion Batteries: Challenges and Opportunities, *Chem. Mater.*, 2017, **29**(12), 5031–5042, DOI: 10.1021/acs.chemmater.7b01764.

12 X. Zou, P. Xiong, J. Zhao, J. Hu, Z. Liu and Y. Xu, Recent Research Progress in Non-Aqueous Potassium-Ion Batteries, *Phys. Chem. Chem. Phys.*, 2017, **19**(39), 26495–26506, DOI: 10.1039/c7cp03852f.

13 I. Hasa, J. Hassoun and S. Passerini, Nanostructured Na-Ion and Li-Ion Anodes for Battery Application: A Comparative Overview, *Nano Res.*, 2017, **10**(12), 3942–3969, DOI: 10.1007/s12274-017-1513-7.

14 M. Dahbi, N. Yabuuchi, K. Kubota, K. Tokiwa and S. Komaba, Negative Electrodes for Na-Ion Batteries, *Phys. Chem. Chem. Phys.*, 2014, **16**(29), 15007–15028, DOI: 10.1039/c4cp00826j.

15 I. Hasa, R. Verrelli and J. Hassoun, Transition Metal Oxide–Carbon Composites as Conversion Anodes for Sodium-Ion Battery, *Electrochim. Acta*, 2015, **173**, 613–618, DOI: 10.1016/j.electacta.2015.05.107.

16 H. Zhang, I. Hasa, D. Buchholz, B. Qin and S. Passerini, Effects of Nitrogen Doping on the Structure and Performance of Carbon Coated $Na_3V_2(PO_4)_3$ Cathodes for Sodium-Ion Batteries, *Carbon*, 2017, **124**, 334–341, DOI: 10.1016/j.carbon.2017.08.063.

17 I. Hasa, D. Buchholz, S. Passerini and J. Hassoun, A Comparative Study of Layered Transition Metal Oxide Cathodes for Application in Sodium-Ion Battery, *ACS Appl. Mater. Interfaces*, 2015, **7**(9), 5206–5212, DOI: 10.1021/am5080437.

18 M. H. Han, E. Gonzalo, G. Singh and T. Rojo, A Comprehensive Review of Sodium Layered Oxides: Powerful Cathodes for Na-Ion Batteries, *Energy Environ. Sci.*, 2015, **8**(1), 81–102, DOI: 10.1039/c4ee03192j.

19 C. Masquelier and L. Croguennec, Polyanionic (Phosphates, Silicates, Sulfates) Frameworks as Electrode Materials for Rechargeable Li (or Na) Batteries, *Chem. Rev.*, 2013, **113**(8), 6552–6591, DOI: 10.1021/cr3001862.

20 I. Hasa, S. Passerini and J. Hassoun, Characteristics of an Ionic Liquid Electrolyte for Sodium-Ion Batteries, *J. Power Sources*, 2016, **303**, 203–207, DOI: 10.1016/j.jpowsour.2015.10.100.

21 S. Komaba, W. Murata, T. Ishikawa, N. Yabuuchi, T. Ozeki, T. Nakayama, A. Ogata, K. Gotoh and K. Fujiwara, Electrochemical Na Insertion and Solid Electrolyte Interphase for Hard-Carbon Electrodes and Application to Na-Ion Batteries, *Adv. Funct. Mater.*, 2011, **21**(20), 3859–3867, DOI: 10.1002/adfm.201100854.

22 D. Monti, E. Jónsson, M. R. Palacín and P. Johansson, Ionic Liquid Based Electrolytes for Sodium-Ion Batteries: Na^+ Solvation and Ionic Conductivity, *J. Power Sources*, 2014, **245**, 630–636, DOI: 10.1016/j.jpowsour.2013.06.153.

23 A. Ponrouch, D. Monti, A. Boschin, B. Steen, P. Johansson and M. R. Palacín, Non-Aqueous Electrolytes for Sodium-Ion Batteries, *J. Mater. Chem. A*, 2015, **3**(1), 22–42, DOI: 10.1039/c4ta04428b.

24 A. Ponrouch, E. Marchante, M. Courty, J. Tarascon and M. R. Palacin, In Search of an Optimized Electrolyte for Na-Ion Batteries, *Energy Environ. Sci.*, 2012, **5**, 8572–8583, DOI: 10.1039/c2ee22258b.

25 Y. Okamoto, Density Functional Theory Calculations of Alkali Metal (Li, Na, and K) Graphite Intercalation Compounds, *J. Phys. Chem. C*, 2014, **118**(1), 16–19, DOI: 10.1021/jp4063753.

26 P. Ge and M. Fouletier, Electrochemical Intercalation of Sodium in Graphite, *Solid State Ionics*, 1988, **28-30**, 1172–1175, DOI: 10.1016/0167-2738(88)90351-7.

27 K. Nobuhara, H. Nakayama, M. Nose, S. Nakanishi and H. Iba, First-Principles Study of Alkali Metal-Graphite Intercalation Compounds, *J. Power Sources*, 2013, **243**, 585–587, DOI: 10.1016/j.jpowsour.2013.06.057.

28 Y. Liu, B. V. Merinov and W. A. Goddard, Origin of Low Sodium Capacity in Graphite and Generally Weak Substrate Binding of Na and Mg among Alkali and Alkaline Earth Metals, *Proc. Natl. Acad. Sci. U. S. A.*, 2016, **113**(14), 3735–3739, DOI: 10.1073/pnas.1602473113.

29 H. Hou, X. Qiu, W. Wei, Y. Zhang and X. Ji, Carbon Anode Materials for Advanced Sodium-Ion Batteries, *Adv. Energy Mater.*, 2017, **7**(24), 1602898, DOI: 10.1002/aenm.201602898.

30 B. Xiao, T. Rojo and X. Li, Hard Carbon as Sodium-Ion Battery Anodes: Progress and Challenges, *ChemSusChem*, 2019, **12**(1), 133–144, DOI: 10.1002/cssc.201801879.

31 M. Wahid, D. Puthusseri, Y. Gawli, N. Sharma and S. Ogale, Hard Carbons for Sodium-Ion Battery Anodes: Synthetic Strategies, Material Properties, and Storage Mechanisms, *ChemSusChem*, 2018, **11**(3), 506–526, DOI: 10.1002/cssc.201701664.

32 K. Lei, F. Li, C. Mu, J. Wang, Q. Zhao, C. Chen and J. Chen, High K-Storage Performance Based on the Synergy of Dipotassium Terephthalate and Ether-Based Electrolytes, *Energy Environ. Sci.*, 2017, **10**(2), 552–557, DOI: 10.1039/c6ee03185d.

33 M. Okoshi, Y. Yamada, S. Komaba, A. Yamada and H. Nakai, Theoretical Analysis of Interactions between Potassium Ions and Organic Electrolyte Solvents: A Comparison with Lithium, Sodium, and Magnesium Ions, *J. Electrochem. Soc.*, 2017, **164**(2), A54–A60, DOI: 10.1149/2.0211702jes.

34 X. Dou, I. Hasa, D. Saurel, C. Vaalma, L. Wu, D. Buchholz, D. Bresser, S. Komaba and S. Passerini, Hard Carbons for Sodium-Ion Batteries: Structure, Analysis, Sustainability, and Electrochemistry, *Mater. Today*, 2019, **23**, 87–104, DOI: 10.1016/j.mattod.2018.12.040.

35 H. Zhang, Y. Huang, H. Ming, G. Cao, W. Zhang, J. Ming and R. Chen, Recent Advances in Nanostructured Carbon for Sodium–Ion Batteries, *J. Mater. Chem. A*, 2020, **8**(4), 1604–1630, DOI: 10.1039/c9ta09984k.

36 Z. Jian, Z. Xing, C. Bommier, Z. Li and X. Ji, Hard Carbon Microspheres: Potassium-Ion Anode Versus Sodium-Ion Anode, *Adv. Energy Mater.*, 2016, **6**(3), 1501874, DOI: 10.1002/aenm.201501874.

37 Z. Jian, W. Luo and X. Ji, Carbon Electrodes for K-Ion Batteries, *J. Am. Chem. Soc.*, 2015, **137**(36), 11566–11569, DOI: 10.1021/jacs.5b06809.

38 T. Chen, L. Pan, T. Lu, C. Fu, D. H. C. Chua and Z. Sun, Fast Synthesis of Carbon Microspheres via a Microwave-Assisted Reaction for Sodium Ion Batteries, *J. Mater. Chem. A*, 2014, **2**(5), 1263–1267, DOI: 10.1039/c3ta14037g.

39 S. Zhang, L. Zhang, L. Qian, J. Yang, Z. Ao and W. Liu, Facile, Sustainable, and Chemical-Additive-Free Synthesis of Monodisperse Carbon Spheres Assisted by External Pressure, *ACS Sustainable Chem. Eng.*, 2019, **7**(8), 7486–7490, DOI: 10.1021/acssuschemeng.9b00036.

40 Z. Li, Y. Chen, Z. Jian, H. Jiang, J. J. Razink, W. F. Stickle, J. C. Neuefeind and X. Ji, Defective Hard Carbon Anode for Na-Ion Batteries, *Chem. Mater.*, 2018, **30**(14), 4536–4542, DOI: 10.1021/acs.chemmater.8b00645.

41 V. Sridhar and H. Park, Sugar-Derived Disordered Carbon Nano-Sheets as High-Performance Electrodes in Sodium-Ion Batteries, *New J. Chem.*, 2017, **41**(11), 4286–4290, DOI: 10.1039/c6nj03917k.

42 Y. Li, S. Xu, X. Wu, J. Yu, Y. Wang, Y. S. Hu, H. Li, L. Chen and X. Huang, Amorphous Monodispersed Hard Carbon Micro-Spherules Derived from Biomass as a High Performance Negative Electrode Material for Sodium-Ion Batteries, *J. Mater. Chem. A*, 2015, **3**(1), 71–77, DOI: 10.1039/c4ta05451b.

43 K. Xu, Q. Pan, F. Zheng, G. Zhong, C. Wang, S. Wu and C. Yang, Hierarchical Nitrogen-Doped Porous Carbon Microspheres as Anode for High Performance Sodium Ion Batteries, *Front. Chem.*, 2019, **7**, 1–8, DOI: 10.3389/fchem.2019.00733.

44 H. L. Wang, Z. Q. Shi, J. Jin, C. B. Chong and C. Y. Wang, Properties and Sodium Insertion Behavior of Phenolic Resin-Based Hard Carbon Microspheres Obtained by a Hydrothermal Method, *J. Electroanal. Chem.*, 2015, **755**, 87–91, DOI: 10.1016/j.jelechem.2015.07.032.

45 Q. Meng, Y. Lu, F. Ding, Q. Zhang, L. Chen and Y. S. Hu, Tuning the Closed Pore Structure of Hard Carbons with the Highest Na Storage Capacity, *ACS Energy Lett.*, 2019, **4**(11), 2608–2612, DOI: 10.1021/acsenergylett.9b01900.

46 K. Tang, L. Fu, R. J. White, L. Yu, M. M. Titirici, M. Antonietti and J. Maier, Hollow Carbon Nanospheres with Superior Rate Capability for Sodium-Based Batteries,

Adv. Energy Mater., 2012, **2**(7), 873–877, DOI: 10.1002/aenm.201100691.

47 Y. Morikawa, S. Nishimura, R. Hashimoto, M. Ohnuma and A. Yamada, Mechanism of Sodium Storage in Hard Carbon: An X-Ray Scattering Analysis, *Adv. Energy Mater.*, 2020, **10**(3), 1903176, DOI: 10.1002/aenm.201903176.

48 Y. Z. Jin, C. Gao, W. K. Hsu, Y. Zhu, A. Huczko, M. Bystrzejewski, M. Roe, C. Y. Lee, S. Acquah, H. Kroto and D. R.M. Large-Scale Walton, Synthesis and Characterization of Carbon Spheresprepared by Direct Pyrolysis of Hydrocarbons, *Carbon*, 2005, **43**, 1944–1953, DOI: 10.1016/j.carbon.2005.03.002.

49 Q. Zhang, X. Deng, M. Ji, Y. Li and Z. Shi, Hard Carbon Microspheres Derived from Resorcinol Formaldehyde Resin as High-Performance Anode Materials for Sodium-Ion Battery, *Ionics*, 2020, **26**, 4523–4532, DOI: 10.1007/s11581-020-03585-7.

50 G. G. Gaddam, D. Yang, R. Narayan, K. V. S. N. Raju, N. A. Kumar and X. S. Zhao, Biomass Derived Carbon Nanoparticle as Anodes for High Performance Sodium and Lithium Ion Batteries, *Nano Energy*, 2016, **26**, 346–352, DOI: 10.1016/j.nanoen.2016.05.047.

51 L. Ji, Z. Lin, M. Alcoutlabi and X. Zhang, Recent Developments in Nanostructured Anode Materials for Rechargeable Lithium-Ion Batteries, *Energy Environ. Sci.*, 2011, **4**(8), 2682–2689, DOI: 10.1039/c0ee00699h.

52 L. Yang, M. Hu, Q. Lv, H. Zhang, W. Yang and R. Lv, Salt and Sugar Derived High Power Carbon Microspheres Anode with Excellent Low-Potential Capacity, *Carbon*, 2020, **163**, 288–296, DOI: 10.1016/j.carbon.2020.03.021.

53 R. Vali, A. Janes, T. Thomberg and E. Lust, Synthesis and Characterization of D-Glucose Derived Nanospheric Hard Carbon Negative Electrodes for Lithium- and Sodium-Ion Batteries, *Electrochim. Acta*, 2017, **253**(1), 536–544, DOI: 10.1016/j.electacta.2017.09.094.

54 S. Qiu, L. Xiao, M. L. Sushko, K. S. Han, Y. Shao, M. Yan, X. Liang, L. Mai, J. Feng, Y. Cao, X. Ai, H. Yang and J. Liu, Manipulating Adsorption–Insertion Mechanisms in Nanostructured Carbon Materials for High-Efficiency Sodium Ion Storage, *Adv. Energy Mater.*, 2017, **7**(17), 1–11, DOI: 10.1002/aenm.201700403.

55 Y. Dong and Yu Caiyen, *et al.*, Nitrogen-doped carbon microsphere derived from oatmeal as high capacity and superior long life anode material for soidum ion battery, *Electrochim. Acta*, 2016, **191**, 385–391, DOI: 10.1016/j.electacta.2016.01.105.

56 Q. Wei, Y. Fu, G. Zhang, Y. Wang, X. Wang, M. Mohamedi and S. Sun, Highly-Ordered Microporous Carbon Nanospheres: A Promising Anode for High-Performance Sodium-Ion Batteries, *RSC Adv.*, 2016, **6**(87), 84149–84154, DOI: 10.1039/c6ra19393e.

57 R. Kali, B. Padya, T. N. Rao and P. K. Jain, Solid Waste-Derived Carbon as Anode for High Performance Lithium-Ion Batteries, *Diamond Relat. Mater.*, 2019, **98**, 107517, DOI: 10.1016/j.diamond.2019.107517.

58 V. G. Pol, E. Lee, D. Zhou, F. Dogan, J. M. Calderon-Moreno and C. S. Johnson, Spherical Carbon as a New High-Rate Anode for Sodium-Ion Batteries, *Electrochim. Acta*, 2014, **127**, 61–67, DOI: 10.1016/j.electacta.2014.01.132.

59 Z. Li, C. Bommier, Z. S. Chong, Z. Jian, T. W. Surta, X. Wang, Z. Xing, J. C. Neuefeind, W. F. Stickle, M. Dolgos, P. A. Greaney and X. Ji, Mechanism of Na-Ion Storage in Hard Carbon Anodes Revealed by Heteroatom Doping, *Adv. Energy Mater.*, 2017, **7**(18), 1602894, DOI: 10.1002/aenm.201602894.

60 N. Sharma, W. K. Pang, Z. Guo and V. K. Peterson, In Situ Powder Diffraction Studies of Electrode Materials in Rechargeable Batteries, *ChemSusChem*, 2015, **8**(17), 2826–2853, DOI: 10.1002/cssc.201500152.

61 M. Morcrette, Y. Chabre, G. Vaughan, G. Amatucci, J. B. Leriche, S. Patoux, C. Masquelier and J. M. Tarascon, *In Situ* X-Ray Diffraction Techniques as a Powerful Tool to Study Battery Electrode Materials, *Electrochim. Acta*, 2002, **47**(19), 3137–3149, DOI: 10.1016/S0013-4686(02)00233-5.

62 A. C. Ferrari, Raman Spectroscopy of Graphene and Graphite: Disorder, Electron-Phonon Coupling, Doping and Nonadiabatic Effects, *Solid State Commun.*, 2007, **143**, 45–57, DOI: 10.1016/j.ssc.2007.03.052.

63 A. Ferrari and J. Robertson, Interpretation of Raman Spectra of Disordered and Amorphous Carbon, *Phys. Rev. B: Condens. Matter Mater. Phys.*, 2000, **61**(20), 14095–14107, DOI: 10.1103/PhysRevB.61.14095.

64 Y. Jin, S. Sun, M. Ou, Y. Liu, C. Fan, X. Sun, J. Peng, Y. Li, Y. Qiu, P. Wei, Z. Deng, Y. Xu, J. Han and Y. Huang, High-Performance Hard Carbon Anode: Tunable Local Structures and Sodium Storage Mechanism, *ACS Appl. Energy Mater.*, 2018, **1**(5), 2295–2305, DOI: 10.1021/acsaem.8b00354.

65 K. Wang, Y. Xu, Y. Li, V. Dravid, J. Wu and Y. Huang, Sodium Storage in Hard Carbon with Curved Graphene Platelets as the Basic Structural Units, *J. Mater. Chem. A*, 2019, **7**(7), 3327–3335, DOI: 10.1039/C8TA11510A.

66 S. W. Zhang, W. Lv, C. Luo, C. H. You, J. Zhang, Z. Z. Pan, F. Y. Kang and Q. H. Yang, Commercial Carbon Molecular Sieves as a High Performance Anode for Sodium-Ion Batteries, *Energy Storage Mater.*, 2016, **3**, 18–23, DOI: 10.1016/j.ensm.2015.12.004.

67 M. Thommes, K. Kaneko, A. V. Neimark, J. P. Olivier, F. Rodriguez-Reinoso, J. Rouquerol and K. S. W. Sing, Physisorption of Gases, with Special Reference to the Evaluation of Surface Area and Pore Size Distribution (IUPAC Technical Report), *Pure Appl. Chem.*, 2015, **87**(9–10), 1051–1069, DOI: 10.1515/pac-2014-1117.

68 D. A. Stevens and J. R. Dahn, An *In Situ* Small-Angle X-Ray Scattering Study of Sodium Insertion into a Nanoporous Carbon Anode Material within an Operating Electrochemical Cell, *J. Electrochem. Soc.*, 2000, **147**(12), 4428, DOI: 10.1149/1.1394081.

69 D. A. Stevens and J. R. Dahn, The Mechanisms of Lithium and Sodium Insertion in Carbon Materials, *J. Electrochem. Soc.*, 2001, **148**(8), A803, DOI: 10.1149/1.1379565.

70 D. A. Stevens and J. R. Dahn, High Capacity Anode Materials for Rechargeable Sodium-Ion Batteries, *J. Electrochem. Soc.*, 2000, **147**(4), 1271, DOI: 10.1149/1.1393348.

71 E. R. Buiel, A. E. George and J. R. Dahn, Model of Micropore Closure in Hard Carbon Prepared from Sucrose, *Carbon*, 1999, **37**(9), 1399–1407, DOI: 10.1016/S0008-6223(98)00335-2.

72 L. Xiao, Y. Cao, W. A. Henderson, M. L. Sushko, Y. Shao, J. Xiao, W. Wang, M. H. Engelhard, Z. Nie and J. Liu, Hard Carbon Nanoparticles as High-Capacity, High-Stability Anodic Materials for Na-Ion Batteries, *Nano Energy*, 2016, **19**, 279–288, DOI: 10.1016/j.nanoen.2015.10.034.

73 Y. Jiang and J. Liu, Definitions of Pseudocapacitive Materials: A Brief Review, *Energy Environ. Mater.*, 2019, **2**(1), 30–37, DOI: 10.1002/eem2.12028.

74 Z. Jian, C. Bommier, L. Luo, Z. Li, W. Wang, C. Wang, P. A. Greaney and X. Ji, Insights on the Mechanism of Na-Ion Storage in Soft Carbon Anode, *Chem. Mater.*, 2017, **29**(5), 2314–2320, DOI: 10.1021/acs.chemmater.6b05474.

75 C. Bommier, T. W. Surta, M. Dolgos and X. Ji, New Mechanistic Insights on Na-Ion Storage in Nongraphitizable Carbon, *Nano Lett.*, 2015, **15**(9), 5888–5892, DOI: 10.1021/acs.nanolett.5b01969.

76 A. Kamiyama, K. Kubota, T. Nakano, S. Fujimura, S. Shiraishi, H. Tsukada and S. Komaba, High-Capacity Hard Carbon Synthesized from Macroporous Phenolic Resin for Sodium-Ion and Potassium-Ion Battery, *ACS Appl. Energy Mater.*, 2020, **3**(1), 135–140, DOI: 10.1021/acsaem.9b01972.

77 Nagmani and S. Puravankara, Insights into the Plateau Capacity Dependence on the Rate Performance and Cycling Stability of a Superior Hard Carbon Microsphere Anode for Sodium-Ion Batteries, *ACS Appl. Energy Mater.*, 2020, **3**(10), 10045–10052, DOI: 10.1021/acsaem.0c01750.

78 K. Kubota, S. Shimadzu, N. Yabuuchi, S. Tominaka, S. Shiraishi, M. Abreu-Sepulveda, A. Manivannan, K. Gotoh, M. Fukunishi, M. Dahbi and S. Komaba, Structural Analysis of Sucrose-Derived Hard Carbon and Correlation with the Electrochemical Properties for Lithium, Sodium, and Potassium Insertion, *Chem. Mater.*, 2020, **32**(7), 2961–2977, DOI: 10.1021/acs.chemmater.9b05235.

79 S. Huang, Y. Lv, W. Wen, T. Xue, P. Jia, J. Wang, J. Zhang and Y. Zhao, Three-Dimensional Hierarchical Porous Hard Carbon for Excellent Sodium/Potassium Storage and Mechanism Investigation, *Mater. Today Energy*, 2021, **20**, 100673, DOI: 10.1016/j.mtener.2021.100673.

80 B. Zhang, Z. L. Xu, Y. B. He, S. Abouali, M. Akbari Garakani, E. Kamali Heidari, F. Kang and J. K. Kim, Exceptional Rate Performance of Functionalized Carbon Nanofiber Anodes Containing Nanopores Created by (Fe) Sacrificial Catalyst, *Nano Energy*, 2014, **4**, 88–96, DOI: 10.1016/j.nanoen.2013.12.011.

81 E. M. Lotfabad, J. Ding, K. Cui, A. Kohandehghan, W. P. Kalisvaart, M. Hazelton and D. Mitlin, High-Density Sodium and Lithium Ion Battery Anodes from Banana Peels, *ACS Nano*, 2014, **8**(7), 7115–7129, DOI: 10.1021/nn502045y.

82 B. Zhang, Y. Yu, Z. L. Xu, S. Abouali, M. Akbari, Y. B. He, F. Kang and J. K. Kim, Correlation between Atomic Structure and Electrochemical Performance of Anodes Made from Electrospun Carbon Nanofiber Films, *Adv. Energy Mater.*, 2014, **4**(7), 1–9, DOI: 10.1002/aenm.201301448.

83 Q. Wang, C. Gao, W. Zhang, S. Luo, M. Zhou, Y. Liu, R. Liu, Y. Zhang, Z. Wang and A. Hao, Biomorphic Carbon Derived from Corn Husk as a Promising Anode Materials for Potassium Ion Battery, *Electrochim. Acta*, 2019, **324**, 134902, DOI: 10.1016/j.electacta.2019.134902.

84 J. Hu, Y. Xie, M. Yin and Z. Zhang, Nitrogen Doping and Graphitization Tuning Coupled Hard Carbon for Superior Potassium-Ion Storage, *J. Energy Chem.*, 2020, **49**, 327–334, DOI: 10.1016/j.jechem.2020.03.005.

85 C. Liu, N. Xiao, H. Li, Q. Dong, Y. Wang, H. Li, S. Wang, X. Zhang and J. Qiu, Nitrogen-Doped Soft Carbon Frameworks Built of Well-Interconnected Nanocapsules Enabling a Superior Potassium-Ion Batteries Anode, *Chem. Eng. J.*, 2020, **382**, 121759, DOI: 10.1016/j.cej.2019.05.120.

86 X. Lin, J. Huang and B. Zhang, Correlation between the Microstructure of Carbon Materials and Their Potassium Ion Storage Performance, *Carbon*, 2019, **143**, 138–146, DOI: 10.1016/j.carbon.2018.11.001.

87 F. Huang, W. Liu, Q. Wang, F. Wang, Q. Yao, D. Yan, H. Xu, B. Y. Xia and J. Deng, Natural N/O-Doped Hard Carbon for High Performance K-Ion Hybrid Capacitors, *Electrochim. Acta*, 2020, **354**, 136701, DOI: 10.1016/j.electacta.2020.136701.

88 Q. Sun, D. Li, J. Cheng, L. Dai, J. Guo, Z. Liang and L. Ci, Nitrogen-Doped Carbon Derived from Pre-Oxidized Pitch for Surface Dominated Potassium-Ion Storage, *Carbon*, 2019, **155**, 601–610, DOI: 10.1016/j.carbon.2019.08.059.

89 Y. Liu, H. Dai, L. Wu, W. Zhou, L. He, W. Wang, W. Yan, Q. Huang, L. Fu and Y. Wu, A Large Scalable and Low-Cost Sulfur/Nitrogen Dual-Doped Hard Carbon as the Negative Electrode Material for High-Performance Potassium-Ion Batteries, *Adv. Energy Mater.*, 2019, **9**(34), 1–9, DOI: 10.1002/aenm.201901379.

90 J. Yang, Z. Ju, Y. Jiang, Z. Xing, B. Xi, J. Feng and S. Xiong, Enhanced Capacity and Rate Capability of Nitrogen/Oxygen Dual-Doped Hard Carbon in Capacitive Potassium-Ion Storage, *Adv. Mater.*, 2018, **30**(4), 1–11, DOI: 10.1002/adma.201700104.

91 W. Li, Z. Li, C. Zhang, W. Liu, C. Han, B. Yan, S. An and X. Qiu, Hard Carbon Derived from Rice Husk as Anode Material for High Performance Potassium-Ion Batteries, *Solid State Ionics*, 2020, **351**, 115319, DOI: 10.1016/j.ssi.2020.115319.

92 Z. Wu, L. Wang, J. Huang, J. Zou, S. Chen, H. Cheng, C. Jiang, P. Gao and X. Niu, Loofah-Derived Carbon as an Anode Material for Potassium Ion and Lithium Ion Batteries, *Electrochim. Acta*, 2019, **306**, 446–453, DOI: 10.1016/j.electacta.2019.03.165.

93 L. Tao, L. Liu, R. Chang, H. He, P. Zhao and J. Liu, Structural and Interface Design of Hierarchical Porous Carbon Derived from Soybeans as Anode Materials for Potassium-Ion Batteries, *J. Power Sources*, 2020, **463**, 228172, DOI: 10.1016/j.jpowsour.2020.228172.

94 Y. Huang, Y. Wang, P. Bai and Y. Xu, Storage Mechanism of Alkali Metal Ions in the Hard Carbon Anode: An Electrochemical Viewpoint, *ACS Appl. Mater. Interfaces*, 2021, **13**(32), 38441–38449, DOI: 10.1021/acsami.1c12150.

95 N. Sun, Z. Guan, Y. Liu, Y. Cao, Q. Zhu, H. Liu, Z. Wang, P. Zhang and B. Xu, Extended ''Adsorption–Insertion'' Model: A New Insight into the Sodium Storage Mechanism of Hard Carbons, *Adv. Energy Mater.*, 2019, **9**(32), 1–14, DOI: 10.1002/aenm.201901351.

96 Y. Wen, K. He, Y. Zhu, F. Han, Y. Xu, I. Matsuda, Y. Ishii, J. Cumings and C. Wang, Expanded Graphite as Superior Anode for Sodium-Ion Batteries, *Nat. Commun.*, 2014, 5, DOI: 10.1038/ncomms5033.

97 X. Wang, C. Liang and S. Dai, Facile Synthesis of Ordered Mesoporous Carbons with High Thermal Stability by Self-Assembly of Resorcinol-Formaldehyde and Block Copolymers under Highly Acidic Conditions, *Langmuir*, 2008, **24**(14), 7500–7505, DOI: 10.1021/la800529v.

98 X. Zhu, S. Wang, W. Huang, Y. Tian and X. Wang, Controllable Synthesis of Mesoporous Carbon Nanospheres with Uniform Size by a Facile One-Pot Aqueous Strategy under Highly Acidic Conditions, *Carbon*, 2016, **105**, 521–528, DOI: 10.1016/j.carbon.2016.04.079.

99 J. Liu, T. Yang, D. W. Wang, G. Q. Lu, D. Zhao and S. Z. Qiao, A Facile Soft-Template Synthesis of Mesoporous Polymeric and Carbonaceous Nanospheres, *Nat. Commun.*, 2013, **4**, 1–7, DOI: 10.1038/ncomms3798.

100 J. Wang, H. Liu, J. Diao, X. Gu, H. Wang, J. Rong, B. Zong and D. S. Su, Size-Controlled Nitrogen-Containing Mesoporous Carbon Nanospheres by One-Step Aqueous Self-Assembly Strategy, *J. Mater. Chem. A*, 2015, **3**(5), 2305–2313, DOI: 10.1039/c4ta05820h.

101 M. Li, W. Li and S. Liu, Control of the Morphology and Chemical Properties of Carbon Spheres Prepared from Glucose by a Hydrothermal Method, *J. Mater. Res.*, 2012, **27**(8), 1117–1123, DOI: 10.1557/jmr.2011.447.

102 V. G. Pol, J. Wen, K. C. Lau, S. Callear, D. T. Bowron, C. K. Lin, S. A. Deshmukh, S. Sankaranarayanan, L. A. Curtiss, W. I. F. David, D. J. Miller and M. M. Thackeray, Probing the Evolution and Morphology of Hard Carbon Spheres, *Carbon*, 2014, **68**, 104–111, DOI: 10.1016/j.carbon.2013.10.059.

103 R. Alcántara, P. Lavela, G. F. Ortiz and J. L. Tirado, Carbon Microspheres Obtained from Resorcinol-Formaldehyde as High-Capacity Electrodes for Sodium-Ion Batteries, *Electrochem. Solid-State Lett.*, 2005, **8**(4), 225–228, DOI: 10.1149/1.1870612.

104 H. D. Asfaw, C. W. Tai, M. Valvo and R. Younesi, Facile Synthesis of Hard Carbon Microspheres from Polyphenols for Sodium-Ion Batteries: Insight into Local Structure and Interfacial Kinetics, *Mater. Today Energy*, 2020, **18**, 100505, DOI: 10.1016/j.mtener.2020.100505.

105 G. Hasegawa, K. Kanamori, N. Kannari, J. I. Ozaki, K. Nakanishi and T. Abe, Studies on Electrochemical Sodium Storage into Hard Carbons with Binder-Free Monolithic Electrodes, *J. Power Sources*, 2016, **318**, 41–48, DOI: 10.1016/j.jpowsour.2016.04.013.

106 L. Xiao, H. Lu, Y. Fang, M. L. Sushko, Y. Cao, X. Ai, H. Yang and J. Liu, Low-Defect and Low-Porosity Hard Carbon with High Coulombic Efficiency and High Capacity for Practical Sodium Ion Battery Anode, *Adv. Energy Mater.*, 2018, **8**(20), 1703238, DOI: 10.1002/aenm.201703238.

107 G. Yasin, M. Arif, T. Mehtab, M. Shakeel, M. A. Mushtaq, A. Kumar, T. A. Nguyen, Y. Slimani, M. T. Nazir and H. Song, A Novel Strategy for the Synthesis of Hard Carbon Spheres Encapsulated with Graphene Networks as a Low-Cost and Large-Scalable Anode Material for Fast Sodium Storage with an Ultralong Cycle Life, *Inorg. Chem. Front.*, 2020, **7**(2), 402–410, DOI: 10.1039/c9qi01105f.

108 H. Tang, M. Wang, T. Lu and L. Pan, Porous Carbon Spheres as Anode Materials for Sodium-Ion Batteries with High Capacity and Long Cycling Life, *Ceram. Int.*, 2017, **43**(5), 4475–4482, DOI: 10.1016/j.ceramint.2016.12.098.

109 W. Cao, E. Zhang, J. Wang, Z. Liu, J. Ge, X. Yu, H. Yang and B. Lu, Potato Derived Biomass Porous Carbon as Anode for Potassium Ion Batteries, *Electrochim. Acta*, 2019, 364–370, DOI: 10.1016/j.electacta.2018.10.036.

110 J. Ding, H. Zhang, H. Zhou, J. Feng, X. Zheng, C. Zhong, E. Paek, W. Hu and D. Mitlin, Sulfur-Grafted Hollow Carbon Spheres for Potassium-Ion Battery Anodes, *Adv. Mater.*, 2019, **31**(30), 1–9, DOI: 10.1002/adma.201900429.

111 D. Goonetilleke, J. C. Pramudita, M. Choucair, A. Rawal and N. Sharma, Sodium Insertion/Extraction from Single-Walled and Multi-Walled Carbon Nanotubes: The Differences and Similarities, *J. Power Sources*, 2016, **314**, 102–108, DOI: 10.1016/j.jpowsour.2016.03.014.

112 X. Wang, K. Han, D. Qin, Q. Li, C. Wang, C. Niu and L. Mai, Polycrystalline Soft Carbon Semi-Hollow Microrods as Anode for Advanced K-Ion Full Batteries, *Nanoscale*, 2017, **9**(46), 18216–18222, DOI: 10.1039/c7nr06645g.

113 Z. Jian, S. Hwang, Z. Li, A. S. Hernandez, X. Wang, Z. Xing, D. Su and X. Ji, Hard–Soft Composite Carbon as a Long-Cycling and High-Rate Anode for Potassium-Ion Batteries, *Adv. Funct. Mater.*, 2017, **27**(26), 1–6, DOI: 10.1002/adfm.201700324.

114 F. Xie, Z. Xu, A. C. S. Jensen, H. Au, Y. Lu, V. Araullo-Peters, A. J. Drew, Y. S. Hu and M. M. Titirici, Hard–Soft Carbon Composite Anodes with Synergistic Sodium Storage Performance, *Adv. Funct. Mater.*, 2019, **29**(24), 1901072, DOI: 10.1002/adfm.201901072.

115 Y. Li, Y. S. Hu, M. M. Titirici, L. Chen and X. Huang, Hard Carbon Microtubes Made from Renewable Cotton as High-Performance Anode Material for Sodium-Ion Batteries, *Adv. Energy Mater.*, 2016, **6**(18), 1600659, DOI: 10.1002/aenm.201600659.

116 Z. Xu, F. Xie, J. Wang, H. Au, M. Tebyetekerwa, Z. Guo, S. Yang, Y. S. Hu and M. M. Titirici, All-Cellulose-Based Quasi-Solid-State Sodium-Ion Hybrid Capacitors Enabled by Structural Hierarchy, *Adv. Energy Mater.*, 2019, **29**(39), 1903895, DOI: 10.1002/adfm.201903895.

117 P. Schlee, O. Hosseinaei, D. Baker, A. Landmér, P. Tomani, M. J. Mostazo-López, D. Cazorla-Amorós, S. Herou and M. M. Titirici, From Waste to Wealth: From Kraft Lignin to

Free-Standing Supercapacitors, *Carbon*, 2019, 470–480, DOI: 10.1016/j.carbon.2019.01.035.

118 Y. S. Hu, P. Adelhelm, B. M. Smarsly, S. Hore, M. Antonietti and J. Maier, Synthesis of Hierarchically Porous Carbon Monoliths with Highly Ordered Microstructure and Their Application in Rechargeable Lithium Batteries with High-Rate Capability, *Adv. Funct. Mater.*, 2007, **17**(12), 1873–1878, DOI: 10.1002/adfm.200601152.

119 L. Qie, W. Chen, H. Xu, X. Xiong, Y. Jiang, F. Zou, X. Hu, Y. Xin, Z. Zhang and Y. Huang, Synthesis of Functionalized 3D Hierarchical Porous Carbon for High-Performance Supercapacitors, *Energy Environ. Sci.*, 2013, **6**(8), 2497–2504, DOI: 10.1039/c3ee41638k.

120 N. Jayaprakash, J. Shen, S. S. Moganty, A. Corona and L. A. Archer, Porous Hollow Carbon@sulfur Composites for High-Power Lithium-Sulfur Batteries, *Angew. Chem., Int. Ed.*, 2011, **50**(26), 5904–5908, DOI: 10.1002/anie.201100637.

121 R. Li, Y. Zhou, W. Li, J. Zhu and W. Huang, Structure Engineering in Biomass-Derived Carbon Materials for Electrochemical Energy Storage, *Research*, 2020, **2020**, 1–27, DOI: 10.34133/2020/8685436.

122 C. Falco, N. Baccile and M. M. Titirici, Morphological and Structural Differences between Glucose, Cellulose and Lignocellulosic Biomass Derived Hydrothermal Carbons, *Green Chem.*, 2011, **13**(11), 3273–3281, DOI: 10.1039/c1gc15742f.

123 F. Xie, Z. Xu, Z. Guo and M. Titirici, Hard Carbon for sodium-ion batteries and beyond, *Progress in Energy*, 2020, **2**(4), 042002, DOI: 10.1088/2516-1083/aba5f5.

124 C. Chen, Z. Wang, B. Zhang, L. Miao, J. Cai, L. Peng, Y. Huang, J. Jiang, Y. Huang, L. Zhang and J. Xie, Nitrogen-Rich Hard Carbon as a Highly Durable Anode for High-Power Potassium-Ion Batteries, *Energy Storage Mater.*, 2017, **8**, 161–168, DOI: 10.1016/j.ensm.2017.05.010.

125 W. Li, J. Huang, L. Feng, L. Cao, Y. Ren, R. Li, Z. Xu, J. Li and C. Yao, Controlled Synthesis of Macroscopic Three-Dimensional Hollow Reticulate Hard Carbon as Long-Life Anode Materials for Na-Ion Batteries, *J. Alloys Compd.*, 2017, **716**, 210–219, DOI: 10.1016/j.jallcom.2017.05.062.

126 Y. Lian, W. Xin, M. Zhang, Y. Li, L. Yang, Y. Guo and S. Xu, Low-Content Ni-Doped CoS_2 Embedded within N,P-Codoped Biomass-Derived Carbon Spheres for Enhanced Lithium/Sodium Storage, *J. Mater. Sci.*, 2019, **54**(11), 8504–8514, DOI: 10.1007/s10853-019-03416-9.

127 B. Yang, J. Wang, Y. Zhu, K. Ji, C. Wang, D. Ruan and Y. Xia, Engineering Hard Carbon with High Initial Coulomb Efficiency for Practical Sodium-Ion Batteries, *J. Power Sources*, 2021, **492**, 229656, DOI: 10.1016/j.jpowsour.2021.229656.

128 Y. Zhang, R. Zhao, Y. Li, X. Zhu, B. Zhang, X. Lang, L. Zhao, B. Jin, Y. Zhu and Q. Jiang, Potassium-Ion Batteries with Novel N, O Enriched Corn Silk-Derived Carbon as Anode Exhibiting Excellent Rate Performance, *J. Power Sources*, 2021, **481**, 228644, DOI: 10.1016/j.jpowsour.2020.228644.

129 J. Jin, Z. Q. Shi and C. Y. Wang, Electrochemical Performance of Electrospun Carbon Nanofibers as Free-Standing and Binder-Free Anodes for Sodium-Ion and Lithium-Ion Batteries, *Electrochim. Acta*, 2014, **141**, 302–310, DOI: 10.1016/j.electacta.2014.07.079.

130 M. Chen, W. Wang, X. Liang, S. Gong, J. Liu, Q. Wang, S. Guo and H. Yang, Sulfur/Oxygen Codoped Porous Hard Carbon Microspheres for High-Performance Potassium-Ion Batteries, *Adv. Energy Mater.*, 2018, **8**(19), 1–9, DOI: 10.1002/aenm.201800171.

131 S. Tian, Y. Wang, T. Cai, D. Kong, D. Wang, H. Ren and W. Xing, Polyaniline-Derived Carbon Nanotubes as Anode Materials for Potassium-Ion Batteries: Insight into the Effect of N-Doping, *Appl. Surf. Sci.*, 2020, **534**, 147635, DOI: 10.1016/j.apsusc.2020.147635.

132 L. Suo, J. Zhu, X. Shen, Y. Wang, X. Han, Z. Chen, Y. Li, Y. Liu, D. Wang and Y. Ma, Hard Carbon Spheres Interconnected by Carbon Nanotubes as High-Performance Anodes for Sodium–Ion Batteries, *Carbon*, 2019, **151**, 1–9, DOI: 10.1016/j.carbon.2019.05.030.

133 S. Wang, Y. Li, F. Ma, X. Wu, P. Zhou, Z. Miao, P. Gao, S. Zhuo and J. Zhou, Phenolic Resin-Based Carbon Microspheres for Potassium Ion Storage, *Appl. Surf. Sci.*, 2020, **506**, 144805, DOI: 10.1016/j.apsusc.2019.144805.

134 H. Zhang, C. Luo, H. He, H. H. Wu, L. Zhang, Q. Zhang, H. Wang and M. S. Wang, Nano-Size Porous Carbon Spheres as a High-Capacity Anode with High Initial Coulombic Efficiency for Potassium-Ion Batteries, *Nanoscale Horiz.*, 2020, **5**(5), 895–903, DOI: 10.1039/d0nh00018c.

135 J. Zhang, D. W. Wang, W. Lv, S. Zhang, Q. Liang, D. Zheng, F. Kang and Q. H. Yang, Achieving Superb Sodium Storage Performance on Carbon Anodes through an Ether-Derived Solid Electrolyte Interphase, *Energy Environ. Sci.*, 2017, **10**(1), 370–376, DOI: 10.1039/c6ee03367a.

136 S. Liu, J. Mao, Q. Zhang, Z. Wang, W. K. Pang, L. Zhang, A. Du, V. Sencadas, W. Zhang and Z. Guo, An Intrinsically Non-flammable Electrolyte for High Performance Potassium Batteries, *Angew. Chem.*, 2019, **59**(9), 3638–3644, DOI: 10.1002/anie.201913174.

137 H. G. Wang, Z. Wu, F. L. Meng, D. L. Ma, X. L. Huang, L. M. Wang and X. B. Zhang, Nitrogen-Doped Porous Carbon Nanosheets as Low-Cost, High-Performance Anode Material for Sodium-Ion Batteries, *ChemSusChem*, 2013, **6**(1), 56–60, DOI: 10.1002/cssc.201200680.

138 Y. Liu and Z. Gao, Heteroatom Doping Combined with Microstructured Carbon to Enhance the Performance of Sodium-Ion Batteries, *Energy Technol.*, 2017, **5**(3), 481–488, DOI: 10.1002/ente.201600355.

139 S. M. Hong, V. Etacheri, C. N. Hong, S. W. Choi, K. B. Lee and V. G. Pol, Enhanced Lithium- and Sodium-Ion Storage in an Interconnected Carbon Network Comprising Electronegative Fluorine, *ACS Appl. Mater. Interfaces*, 2017, **9**(22), 18790–18798, DOI: 10.1021/acsami.7b03456.

140 H. Song, N. Li, H. Cui and C. Wang, Enhanced Storage Capability and Kinetic Processes by Pores- and Hetero-Atoms- Riched Carbon Nanobubbles for Lithium-Ion and Sodium-Ion Batteries Anodes, *Nano Energy*, 2014, 81–87, DOI: 10.1016/j.nanoen.2013.12.017.

141 J. Yang, X. Zhou, D. Wu, X. Zhao and Z. Zhou, S-Doped N-Rich Carbon Nanosheets with Expanded Interlayer Distance as Anode Materials for Sodium-Ion Batteries, *Adv. Mater.*, 2017, **29**(6), 1604108, DOI: 10.1002/adma.201604108.

142 Y. Qiao, M. Ma, Y. Liu, R. Han, X. Cheng, Q. Li, X. Li, H. Dong, Y. Yin and S. Yang, Tailoring the Sodium Storage Performance of Carbon Nanowires by Microstructure Design and Surface Modification with N, O and S Heteroatoms, *ChemElectroChem*, 2017, **4**(11), 2877–2883, DOI: 10.1002/celc.201700554.

143 Z. Li, L. Ma, T. W. Surta, C. Bommier, Z. Jian, Z. Xing, W. F. Stickle, M. Dolgos, K. Amine, J. Lu, T. Wu and X. Ji, High Capacity of Hard Carbon Anode in Na-Ion Batteries Unlocked by POx Doping, *ACS Energy Lett.*, 2016, **1**(2), 395–401, DOI: 10.1021/acsenergylett.6b00172.

144 X. Zhong, Y. Li, L. Zhang, J. Tang, X. Li, C. Liu, M. Shao, Z. Lu, H. Pan and B. Xu, High-Performance Sodium-Ion Batteries Based on Nitrogen-Doped Mesoporous Carbon Spheres with Ultrathin Nanosheets, *ACS Appl. Mater. Interfaces*, 2019, **11**(3), 2970–2977, DOI: 10.1021/acsami.8b17473.

145 A. Agarwal, S. Janakiraman, K. Biswas, A. Venimadahv, S. K. Srivastava and S. Ghosh, Understanding the Improved Electrochemical Performance of Nitrogen-Doped Hard Carbons as an Anode for Sodium Ion Battery, *Electrochim. Acta*, 2019, **317**, 164–172, DOI: 10.1016/j.electacta.2019.05.158.

146 D. Li, H. Chen, G. Liu, M. Wei, L. X. Ding, S. Wang and H. Wang, Porous Nitrogen Doped Carbon Sphere as High Performance Anode of Sodium-Ion Battery, *Carbon*, 2015, **94**, 888–894, DOI: 10.1016/j.carbon.2015.07.067.

147 H. Tang, D. Yan, T. Lu and L. Pan, Sulfur-Doped Carbon Spheres with Hierarchical Micro/mesopores as Anode Materials for Sodium-Ion Batteries, *Electrochim. Acta*, 2017, **241**, 63–72, DOI: 10.1016/j.electacta.2017.04.112.

148 J. Ye, J. Zang, Z. Tian, M. Zheng and Q. Dong, Sulfur and Nitrogen Co-Doped Hollow Carbon Spheres for Sodium-Ion Batteries with Superior Cyclic and Rate Performance, *J. Mater. Chem. A*, 2016, **4**(34), 13223–13227, DOI: 10.1039/c6ta04592h.

149 F. Zhand, D. Qin, J. Xu, Z. Liu, Y. Zhao and Z. Zhang, Nitrogen and Oxygen Co-Doping Carbon Microspheres by a Sustainable Route for Fast Sodium-Ion Batteries, *Electrochim. Acta*, 2019, **303**, 140–147, DOI: 10.1016/j.electacta.2019.02.067.

150 K. Lu, S. Lu, T. Gu, X. Zheng, K. Ke, X. Li and R. Yang, Onium Salts-Derived B and P Dual-Doped Carbon Microspheres as Anode Material for High-Performance Sodium-Ion Batteries, *Electrochem. Commun.*, 2019, **103**, 22–26, DOI: 10.1016/j.elecom.2019.04.011.

151 J. Ruan, X. Wu, Y. Wang, S. Zheng, D. Sun, Y. Song and M. Chen, Nitrogen-Doped Hollow Carbon Nanospheres towards the Application of Potassium Ion Storage, *J. Mater. Chem. A*, 2019, **7**(33), 19305–19315, DOI: 10.1039/c9ta05205d.

152 J. Ge, B. Wang, J. Zhou, S. Liang, A. M. Rao and B. Lu, Hierarchically Structured Nitrogen-Doped Carbon Microspheres for Advanced Potassium Ion Batteries, *ACS Mater. Lett.*, 2020, **2**(7), 853–860, DOI: 10.1021/acsmaterialslett.0c00171.

153 J. Ding, H. Zhang, H. Zhou, J. Feng, X. Zheng, C. Zhong, E. Paek, W. Hu and D. Mitlin, Sulfur-Grafted Hollow Carbon Spheres for Potassium-Ion Battery Anodes, *Adv. Mater.*, 2019, **31**(30), 1900429, DOI: 10.1002/adma.201900429.

154 M. Chen, W. Wang, X. Liang, S. Gong, J. Liu, Q. Wang, S. Guo and H. Yang, Sulfur/Oxygen Codoped Porous Hard Carbon Microspheres for High-Performance Potassium-Ion Batteries, *Adv. Energy Mater.*, 2018, **8**(19), 1800171, DOI: 10.1002/aenm.201800171.

155 A. Bazargan and G. McKay, A Review – Synthesis of Carbon Nanotubes from Plastic Wastes, *Chem. Eng. J.*, 2012, **195**, 377–391, DOI: 10.1016/j.cej.2012.03.077.

156 S. Villagómez-Salas, P. Manikandan, S. F. Acuña Guzmán and V. G. Pol, Amorphous Carbon Chips Li-Ion Battery Anodes Produced through Polyethylene Waste Upcycling, *ACS Omega*, 2018, **3**(12), 17520–17527, DOI: 10.1021/acsomega.8b02290.

157 W. S. Fonseca, X. Meng and D. Deng, Trash to Treasure: Transforming Waste Polystyrene Cups into Negative Electrode Materials for Sodium Ion Batteries, *ACS Sustainable Chem. Eng.*, 2015, **3**(9), 2153–2159, DOI: 10.1021/acssuschemeng.5b00403.

158 V. G. Pol and M. M. Thackeray, Spherical Carbon Particles and Carbon Nanotubes Prepared by Autogenic Reactions: Evaluation as Anodes in Lithium Electrochemical Cells, *Energy Environ. Sci.*, 2011, **4**(5), 1904–1912, DOI: 10.1039/c0ee00256a.

159 U. Kumar, D. Goonetilleke, V. Gaikwad, J. C. Pramudita, R. K. Joshi, N. Sharma and V. Sahajwalla, Activated Carbon from E-Waste Plastics as a Promising Anode for Sodium-Ion Batteries, *ACS Sustainable Chem. Eng.*, 2019, **7**(12), 10310–10322, DOI: 10.1021/acssuschemeng.9b00135.

160 E. Bäckström, K. Odelius and M. Hakkarainen, Trash to Treasure: Microwave-Assisted Conversion of Polyethylene to Functional Chemicals, *Ind. Eng. Chem. Res.*, 2017, **56**(50), 14814–14821, DOI: 10.1021/acs.iecr.7b04091.

161 F. Xie, Z. Xu, A. C. S. Jensen, H. Au, Y. Lu, V. Araullo-Peters, A. J. Drew, Y. S. Hu and M. M. Titirici, Hard–Soft Carbon Composite Anodes with Synergistic Sodium Storage Performance, *Adv. Funct. Mater.*, 2019, **29**(24), 1901072, DOI: 10.1002/adfm.201901072.

162 Y. Guo, J. Li, H. Wang, L. Chang, B. Rui, L. Lin, T. Xu and P. Nie, Aerosol-Assisted Assembly of Mesoporous Carbon Spheres With Fast and Stable K-Ion Storage, *Front. Chem.*, 2020, **8**, 1–9, DOI: 10.3389/fchem.2020.00784.

163 G. Wang, X. Xiong, D. Xie, Z. Lin, J. Zheng, F. Zheng, Y. Li, Y. Liu, C. Yang and M. Liu, Chemically Activated Hollow Carbon Nanospheres as a High-Performance Anode Material for Potassium Ion Batteries, *J. Mater. Chem. A*, 2018, **6**(47), 24317–24323, DOI: 10.1039/c8ta09751h.

164 D. S. Bin, Z. X. Chi, Y. Li, K. Zhang, X. Yang, Y. G. Sun, J. Y. Piao, A. M. Cao and L. J. Wan, Controlling the Compositional Chemistry in Single Nanoparticles for Functional Hollow Carbon Nanospheres, *J. Am. Chem. Soc.*, 2017, **139**(38), 13492–13498, DOI: 10.1021/jacs.7b07027.

165 X. S. Tao, Y. G. Sun, Y. Liu, B. B. Chang, C. T. Liu, Y. S. Xu, X. C. Yang and A. M. Cao, Facile Synthesis of Hollow Carbon Nanospheres and Their Potential as Stable Anode Materials in Potassium-Ion Batteries, *ACS Appl. Mater. Interfaces*, 2020, **12**(11), 13182–13188, DOI: 10.1021/acsami.9b22736.

166 Y. He, J. Xue, M. Yang, T. Huang, X. Xia, Y. Chen and H. Liu, Hollow Carbon Nanospheres for Capacitive-Dominated Potassium-Ion Storage, *Chem. Eng. J.*, 2021, **409**(1), 127383, DOI: 10.1016/j.cej.2020.127383.

167 W. Xiong, J. Zhang, Y. Xiao, Y. Zhu, Z. Wang and Z. Lu, Oxygen-Rich Nanoflake-Interlaced Carbon Microspheres for Potassium-Ion Battery Anodes, *Chem. Commun.*, 2020, **56**(23), 3433–3436, DOI: 10.1039/d0cc00357c.

168 J. Hu, Y. Xie, X. Zhou and Z. Zhang, Engineering Hollow Porous Carbon-Sphere-Confined MoS_2 with Expanded (002) Planes for Boosting Potassium-Ion Storage, *ACS Appl. Mater. Interfaces*, 2020, **12**(1), 1232–1240, DOI: 10.1021/acsami.9b14742.

169 W. Li, M. Zhou, H. Li, K. Wang, S. Cheng and K. Jiang, A High Performance Sulfur-Doped Disordered Carbon Anode for Sodium Ion Batteries, *Energy Environ. Sci.*, 2015, **8**(10), 2916–2921, DOI: 10.1039/c5ee01985k.

170 P. Thomas and D. Billaud, Electrochemical Insertion of Sodium into Hard Carbons, *Electrochim. Acta*, 2002, **47**(20), 3303–3307, DOI: 10.1016/S0013-4686(02)00250-5.

171 S. Huang, Z. Li, B. Wang, J. Zhang, Z. Peng, R. Qi, J. Wang and Y. Zhao, N-Doping and Defective Nanographitic Domain Coupled Hard Carbon Nanoshells for High Performance Lithium/Sodium Storage, *Adv. Funct. Mater.*, 2018, **28**(10), 1–10, DOI: 10.1002/adfm.201706294.

172 M. K. Rybarczyk, Y. Li, M. Qiao, Y. S. Hu, M. M. Titirici and M. Lieder, Hard Carbon Derived from Rice Husk as Low Cost Negative Electrodes in Na-Ion Batteries, *J. Energy Chem.*, 2019, **29**, 17–22, DOI: 10.1016/j.jechem.2018.01.025.

173 Y. Zhu, M. Chen, Q. Li, C. Yuan and C. Wang, High-Yield Humic Acid-Based Hard Carbons as Promising Anode Materials for Sodium-Ion Batteries, *Carbon*, 2017, **123**, 727–734, DOI: 10.1016/j.carbon.2017.08.030.

174 H. Liu, M. Jia, B. Cao, R. Chen, X. Lv, R. Tang, F. Wu and B. Xu, Nitrogen-Doped Carbon/graphene Hybrid Anode Material for Sodium-Ion Batteries with Excellent Rate Capability, *J. Power Sources*, 2016, **319**, 195–201, DOI: 10.1016/j.jpowsour.2016.04.040.

175 H. Y. Yu, H. J. Liang, Z. Y. Gu, Y. F. Meng, M. Yang, M. X. Yu, C. Zhao and X. L. De; Wu, Waste-to-Wealth: Low-Cost Hard Carbon Anode Derived from Unburned Charcoal with High Capacity and Long Cycle Life for Sodium-Ion/Lithium-Ion Batteries, *Electrochim. Acta*, 2020, **361**, 137041, DOI: 10.1016/j.electacta.2020.137041.

176 Y. Zhang, X. Li, P. Dong, G. Wu, J. Xiao, X. Zeng, Y. Zhang and X. Sun, Honeycomb-like Hard Carbon Derived from Pine Pollen as High-Performance Anode Material for Sodium-Ion Batteries, *ACS Appl. Mater. Interfaces*, 2018, **10**(49), 42796–42803, DOI: 10.1021/acsami.8b13160.

177 K. Wang, Y. Jin, S. Sun, Y. Huang, J. Peng, J. Luo, Q. Zhang, Y. Qiu, C. Fang and J. Han, Low-Cost and High-Performance Hard Carbon Anode Materials for Sodium-Ion Batteries, *ACS Omega*, 2017, **2**(4), 1687–1695, DOI: 10.1021/acsomega.7b00259.

178 W. Li, L. Zeng, Z. Yang, L. Gu, J. Wang, X. Liu, J. Cheng and Y. Yu, Free-Standing and Binder-Free Sodium-Ion Electrodes with Ultralong Cycle Life and High Rate Performance Based on Porous Carbon Nanofibers, *Nanoscale*, 2014, **6**(2), 693–698, DOI: 10.1039/c3nr05022j.

179 X. Lin, Y. Liu, H. Tan and B. Zhang, Advanced Lignin-Derived Hard Carbon for Na-Ion Batteries and a Comparison with Li and K Ion Storage, *Carbon*, 2020, **157**, 316–323, DOI: 10.1016/j.carbon.2019.10.045.

180 X. He, J. Liao, Z. Tang, L. Xiao, X. Ding, Q. Hu, Z. Wen and C. Chen, Highly Disordered Hard Carbon Derived from Skimmed Cotton as a High-Performance Anode Material for Potassium-Ion Batteries, *J. Power Sources*, 2018, **396**, 533–541, DOI: 10.1016/j.jpowsour.2018.06.073.